International Journal of Solids and Structures 305 (2024) 113049

Contents lists available at ScienceDirect

International Journal of Solids and Structures

journal homepage: www.elsevier.com/locate/ijsolstr

A novel cohesive interlayer model considering friction

Jiang Yu [a], Bin Gong [b,*], Chenrui Cao [c], Chun'an Tang [d]

[a] School of Resources and Civil Engineering, Northeastern University, Shenyang 110819, China
[b] Department of Civil and Environmental Engineering, Brunel University London, London UB8 3PH, UK
[c] College of Mechanical Engineering, Taiyuan University of Technology, Taiyuan 030024, China
[d] State Key Laboratory of Coastal and Offshore Engineering, Dalian University of Technology, Dalian 116024, China

ARTICLE INFO

Keywords:
Cohesive zone model
Frictional contact
Park-Paulino-Roesler model
Direct shear
Crack propagation

ABSTRACT

To understand the influence of friction on the shear-slip behavior of heterogeneous brittle composites, a novel cohesive interlayer model that can effectively capture the friction effect was proposed based on the classical Park-Paulino-Roesler model. Meanwhile, the unified potential energy function governing the interface tangential and normal behaviors was introduced to realize the mechanical interaction between Mode I fracture and Mode II fracture, and a smooth friction growth function was added in the elastic deformation stage for calculating the accurate contact pressure and friction force. Furthermore, the capability of the proposed model in addressing unloading and reloading was improved, and the fracture energy can vary accordingly during cyclic loading. To verify the effectiveness of the proposed model, it was examined by modelling the shear behavior of a masonry wallette. The results show that the relative error of the proposed model is 14.92% which is much lower than those of the other three pre-existing models when calculating the displacement corresponding to peak shear stress. Meanwhile, in terms of peak shear stress and initial displacement at residual stage, the relative errors of the proposed model are only 1.82% and 5.04%, respectively, indicating the high accuracy. Besides, the tangent stiffness determined by the second-order integration of the potential energy function is also continuous and smooth, which ensures the effective convergence of the proposed cohesive model.

1. Introduction

Cohesion and friction play a considerable role in governing the mechanical behavior of heterogeneous brittle materials, such as concrete, rock and rubble (Tarasov 2023; Wang et al. 2022; Feng et al. 2022). Indeed, the creation, propagation and coalescence of microcracks inside such materials is a continuous to discontinuous process (Gong et al. 2024; Feng et al. 2024; Luo et al. 2023). Meanwhile, the gradual development of multiple cracks is generally accompanied with the action of frictional contacts. The cohesive zone model (Enayatpour et al. 2018; Chen et al. 2020; Yu et al. 2020) has been proposed to simulate the progressive failure of brittle materials using the finite element method (FEM) or the discrete element method (DEM). However, the shearing strength of interlayers inside brittle materials are commonly provided by the combined action of cohesion and friction, which cannot be taken into account by the conventional cohesive zone model in most numerical simulations (Benzeggagh and Kenane 1996; Haddad and Sepehrnoori 2016). Researchers have established several coupling cohesion-friction models in the FEM (Tvergaard 1990). For most of them, friction can only act when the cohesive force disappears completely, which is therefore unreasonable compared with the actual situation. To determine the onset condition of friction, some researchers pointed out that the fraction force can start to act when the cohesion enters the softening stage (Rezazadeh et al. 2017; Dehestani and Mousavi 2015; Jin et al. 2019; Tian et al. 2021). These improved models were mainly applied to simulate the pull-out of reinforcement or steel from concrete and the failure of masonry wall (Bolhassani et al. 2015; Zeng et al. 2021; Sunkpal and Sherizadeh 2022). Additionally, Yao et al. (2015), Li et al. (2017) and Li et al. (2019) used the coupling cohesion-friction model to investigate rock failure.

In 2009, the Park-Paulino-Roesler (PPR) model was proposed by Park et al. (2009) and Park (2009) to model the mechanical response of interlayers. In the following years, researchers added new features to the PPR cohesive model and applied it in engineering practice. Gilormini and Diani (2017) came up with a different linear loading, unloading and reloading relationship coupled with the PPR cohesive model. Oliver et al. (2019) developed a PPR-based cohesive model which can consider the rate-dependent effect. Yang et al. (2021) investigated the fracture

* Corresponding author.
E-mail address: bin.gong@brunel.ac.uk (B. Gong).

https://doi.org/10.1016/j.ijsolstr.2024.113049
Received 23 May 2023; Received in revised form 30 July 2024; Accepted 26 August 2024
Available online 31 August 2024

characteristics of different kinds of concretes by simulating the disk-shaped compact tension (DCT) tests and the punch-through shear (PTS) tests. Zhong et al. (2021) proposed a new model by coupling an unloading/reloading relationship with the PPR-based cohesive model to investigate the interface cracking of a slab track. Tvergaard (1990) proposed a cohesive model considering friction. However, this model assumed that the friction plays a role after the interlayer cohesion is reduced to 0, which leads to the unsmooth conversion between cohesion and friction and the convergence difficulty. To solve this problem, Spring and Paulino (2015) improved the model by calculating the interlayer friction when the cohesion reaches the peak. Although the model can consider the influence of friction and cohesion on shear strength, the peak shear stress will lag when the friction is large because the peak values of cohesion and friction are generally not researched at the same shear deformation. Therefore, their model cannot appropriately characterize the shear strength.

Furthermore, Baek and Park (2018) proposed a model where friction peaks at the initiation of tangential displacement and remains constant under unchanged normal conditions. To reflect this behavior, they simplified the PPR cohesive model by adjusting its traction to reach its maximum when tangential displacement is zero, effectively eliminating its ascending segment. While this adjustment suits dynamic simulations dominated by friction, it can compromise the convergence of numerical calculations in quasi-static scenarios. Moreover, when dealing with interfaces of initially low stiffness, this approach might introduce excessive elastic stiffness. In contrast, Spring and Paulino (2015) chose to preserve the original PPR cohesive model. Instead, they introduced a κ-factor to capture how frictional force varies with relative displacement, assuming it remains at 0 until traction peaks. Although this strategy can introduce a phase difference between traction and friction, it complicates the decomposition of actual interface strength into friction and cohesion when fitting shear strength and friction coefficients. Furthermore, in the model proposed by Li et al. (2017), the relationship between peak shear displacement and cohesion remains uncertain. Additionally, their model neglects the continuous differentiability of both cohesive and frictional terms concerning tangential displacement. Notably, Park et al. (2009) highlighted the pivotal role of continuous differentiability in the traction-displacement equation, significantly enhancing numerical convergence. Hence, ensuring this continuity is imperative in the traction-displacement governing equation. Moreover, considering the non-negligible initial stiffness of the interface is crucial. This factor becomes particularly relevant in characterizing interface deformation under relatively low stiffness during the initial loading stages. Incorporating this aspect effectively can provide deeper insights into the interface behavior and contribute to a more comprehensive understanding of its mechanical response.

In this study, a novel coupling model is proposed to fully describe the interaction of cohesion and frictional contact between two adjacent media based on the PPR cohesive model. In the developed model, the Mode I and Mode II fractures are controlled by a unified potential energy function and can influence each other. Namely, an interactive relationship between these two fracture modes is established. The unified potential energy function is second-order continuous and differentiable with respect to displacement. Therefore, the related stress-displacement curve is continuous and smooth. Besides, the tangent stiffness determined by the second-order integration of the potential energy function is also continuous and smooth, which ensures the effective convergence of the proposed cohesive model compared with the bilinear and trilinear cohesive models (Park and Paulino 2012; Spring and Paulino 2014; Park et al. 2016). The governing function of friction force in the proposed model is continuous and differentiable with respect to the Mode II displacement. Thus, the superposition equation of cohesive and friction can also be continuous and smooth. The continuous growth of friction will not have a negative impact on the convergence of the model.

For the coupling friction-cohesion model, a reasonable unloading/reloading relationship is indispensable. Through the cyclic shear displacement loading, the jumping of friction can be determined (Zhang et al. 2020). During the process of reloading, the influence of previous loading history on traction can be captured. According to these principles, the direct shear test of masonry wallette is carried out, and the results obtained by the proposed model are compared with the experimental data and the numerical simulations by the other methods. After comparison, the effectiveness and reliability of the proposed model are verified, and the satisfactory convenience for parameter fitting are also be confirmed. Through describing the interlayer between steel tube and concrete, we further investigate the effects of the coronal gap length and the angle between loading direction and gap axis on the bending and bearing capacity of circular concrete-filled steel tube (CCFST) under eccentric compression.

2. Methodology

2.1. The basic cohesive model

In 2009, Park et al. (2009) and Park (2009) proposed the PPR cohesive model, for which, each parameter has a clear physical meaning, and the bonding force and tangent stiffness matrix are uniformly controlled by the continuous potential energy function. The normal and tangential cohesions T_n and T_t can be obtained by calculating the first-order derivatives of the normal and tangential displacements of the potential energy function. The Jacobian matrix can be obtained by solving the second-order differential equation of the potential energy function. Because the cohesion-displacement curve is continuous and smooth, the convergence of the numerical iteration of the calculation model can be guaranteed.

The potential energy function of the PPR cohesive model is as follows:

$$\psi(\Delta_n,\Delta_t) = \min(\phi_n,\phi_t) + \left[\Gamma_n\left(1-\frac{\Delta_n}{\delta_n}\right)^{\alpha}\left(\frac{m}{\alpha}+\frac{\Delta_n}{\delta_n}\right)^{m} + \langle\phi_n-\phi_t\rangle\right] \times \left[\Gamma_t\left(1-\frac{|\Delta_t|}{\delta_t}\right)^{\beta}\left(\frac{n}{\beta}+\frac{\Delta_t}{\delta_t}\right)^{n} + \langle\phi_t-\phi_n\rangle\right] \tag{1}$$

where Δ_n and Δ_t are the normal and tangential opening displacements, respectively; ϕ_n and ϕ_t are the Mode I and Mode II fracture energy, respectively; α and β are the parameters controlling the softening form of the normal and tangential cohesions after reaching shear strength. The potential energy function is controlled in a scope with the boundaries of (0,δ_n), ($-\delta_t$,δ_t). δ_n and δ_t are the final opening displacements along the normal and tangential directions, respectively, and be determined by Eq. (2).

$$\begin{cases} \delta_n = \dfrac{\phi_n}{\sigma_{\max}}\alpha\lambda_n(1-\lambda_n)^{\alpha-1}\left(\dfrac{\alpha}{m}+1\right)\left(\dfrac{\alpha}{m}\lambda_n+1\right)^{m-1} \\ \delta_t = \dfrac{\phi_t}{\tau_{\max}}\beta\lambda_t(1-\lambda_t)^{\beta-1}\left(\dfrac{\beta}{n}+1\right)\left(\dfrac{\beta}{n}\lambda_t+1\right)^{n-1} \end{cases} \tag{2}$$

where σ_{max} and τ_{max} are the normal and tangential strengths of interlayer materials, which are also the maximum values regarding cohesion; λ_n and λ_t control the initial normal and tangential stiffnesses of the cohesion displacement curve, which is numerically equal to the displacement ratio when the cohesion reaches the scope boundaries of the potential energy function. The governing equation is shown in Eq. (3).

$$T_n = (\lambda_n\delta_n, 0) = \sigma_{\max}, T_t = (0, \lambda_t\delta_t) = \tau_{\max} \tag{3}$$

The variation of the normal and tangential cohesions subject to the opening displacement is controlled by Eqs. (4) and (5), where T_n and T_t are the normal and tangential cohesions, respectively.

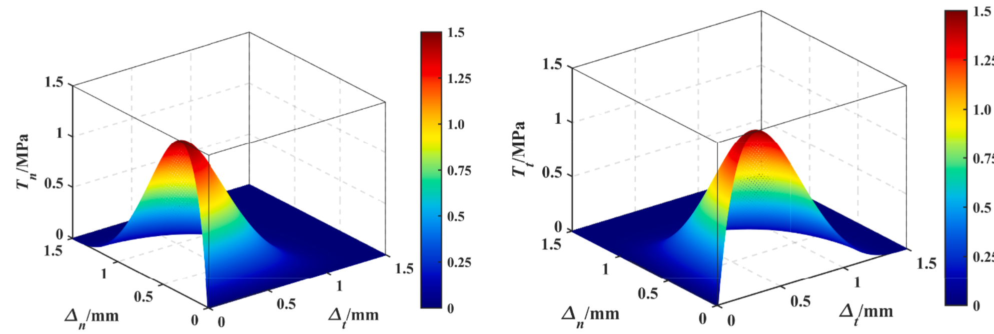

(a) Relationship of displacement-normal cohesion (b) Relationship of displacement-tangential cohesion

Fig. 1. Separation-traction relation of the PPR cohesive model.

$$\begin{cases} T_n(\Delta_n,\Delta_t)=\dfrac{\delta\psi}{\delta\Delta_n}=\dfrac{\Gamma_n}{\delta_n}\left[m\left(1-\dfrac{\Delta_n}{\delta_n}\right)^{\alpha}\left(\dfrac{m}{\alpha}+\dfrac{a_n}{\delta_n}\right)^{m-1}-\alpha\left(1-\dfrac{\Delta_n}{\delta_n}\right)^{\alpha-1}\left(\dfrac{m}{\alpha}+\dfrac{\Delta_n{}^{m}}{\delta_n}\right)\right] \\ \times\left[\Gamma_t\left(1-\dfrac{|\Delta_t|}{\delta_t}\right)^{\beta}\left(\dfrac{n}{\beta}+\dfrac{|\Delta_t|}{\delta_t}\right)^{n}+\langle\phi_t-\phi_n\rangle\right] \\ T_t(\Delta_n,\Delta_t)=\dfrac{\partial\psi}{\partial\Delta_t}=\dfrac{\Gamma_t}{\delta_t}\left[n\left(1-\dfrac{|\Delta_t|}{\delta_t}\right)^{\beta}\left(\dfrac{n}{\beta}+\dfrac{|\Delta_t|}{\delta_t}\right)^{n-1}-\beta\left(1-\dfrac{|\Delta_t|}{\delta_t}\right)^{\beta-1}\left(\dfrac{n}{\beta}+\dfrac{|\Delta_t|}{\delta_t}\right)^{n}\right] \\ \times\left[\Gamma_n\left(1-\dfrac{\Delta_n}{\delta_n}\right)^{\alpha}\left(\dfrac{m}{\alpha}+\dfrac{\Delta_n}{\delta_n}\right)^{m}+\langle\phi_n-\phi_t\rangle\right]\dfrac{\Delta_t}{|\Delta_t|} \end{cases} \tag{4}$$

$$\begin{cases} T_n(\Delta_n,\Delta_t)=\begin{cases} \dfrac{\partial\psi}{\partial\Delta_n}=\dfrac{\Gamma_n}{\delta_n}\left[m\left(1-\dfrac{\Delta_n}{\delta_n}\right)^{\alpha}\left(\dfrac{m}{\alpha}+\dfrac{\Delta_n}{\delta_n}\right)^{m-1}+\alpha\left(1-\dfrac{\Delta_n}{\delta_n}\right)^{\alpha-1}\left(\dfrac{m}{\alpha}+\dfrac{\Delta_n}{\delta_n}\right)^{m}\right]\times\left[\Gamma_t\left(1-\dfrac{|\Delta_t|}{\delta_t}\right)^{\beta}\left(\dfrac{n}{\beta}+\dfrac{|\Delta_t|}{\delta_t}\right)^{n}+\langle\varphi_t-\varphi_n\rangle\right] & \Delta_n\in[0,+\infty) \\ \dfrac{\partial T_n(0,0)}{\partial\Delta_n}\Delta_n=\dfrac{\Gamma_n}{\delta_n^2}\left[(m^2-m)\left(\dfrac{m}{\alpha}\right)^{m-2}+(\alpha^2-\alpha)\left(\dfrac{m}{\alpha}\right)^{m}-2\alpha m\left(\dfrac{m}{\alpha}\right)^{m-1}\right]\times\left[\Gamma_t\left(\dfrac{n}{\beta}\right)^{n}+\langle\varphi_t-\varphi_n\rangle\right]\Delta_n, & \Delta_n\in(-\infty,0) \end{cases} \\ T_t(\Delta_n,\Delta_t)=\dfrac{\partial\psi}{\partial\Delta_t}=\dfrac{\Gamma_t}{\delta_t}\left[n\left(1-\dfrac{|\Delta_t|}{\delta_t}\right)^{\beta}\left(\dfrac{n}{\beta}+\dfrac{|\Delta_t|}{\delta_t}\right)^{n-1}-\beta\left(1-\dfrac{|\Delta_t|}{\delta_t}\right)^{\beta-1}\left(\dfrac{n}{\beta}+\dfrac{|\Delta_t|}{\delta_t}\right)^{n}\right] \\ \times\left[\Gamma_n\left(1-\dfrac{\Delta_n}{\delta_n}\right)^{\alpha}\left(\dfrac{m}{\alpha}+\dfrac{\Delta_n}{\delta_n}\right)^{m}+\langle\phi_n-\phi_t\rangle\right]\dfrac{\Delta_t}{|\Delta_t|} \end{cases} \tag{5}$$

where Γ_n and Γ_t are the normal and tangential fracture energy coefficients, respectively. Note that Eqs. (4) and (5) define the calculation method for cohesions in both tension and compression conditions. When an interface is in tension, the expression for T_n is the partial derivative of the potential function with respect to normal displacement. In compression, according to Spring and Paulino (2015) and Li et al. (2017), T_n increases linearly with the growth of normal displacement. The stiffness in compression state is the initial stiffness of T_n in tensile state and is not influenced by tangential state. When the normal and tangential fracture energy magnitudes are not equal, the fracture energy coefficients can be calculated by Eq. (6)

$$\begin{cases} \Gamma_n=(-\phi_n)^{\langle\phi_n-\phi_t\rangle/(\phi_n-\phi_t)}\left(\dfrac{\alpha}{m}\right)^{m} \\ \Gamma_t=(-\phi_t)^{\langle\phi_t-\phi_n\rangle/(\phi_t-\phi_n)}\left(\dfrac{\beta}{n}\right)^{n} \end{cases} \tag{6}$$

where m and n are two dimensionless constants. When the normal and tangential fracture energy magnitudes are equal, the fracture energy coefficients can be computed by Eq. (7).

$$\begin{cases} \Gamma_n=(-\phi_n)\left(\dfrac{\alpha}{m}\right)^{m} \\ \Gamma_t=\left(\dfrac{\beta}{n}\right)^{n} \end{cases} \tag{7}$$

The calculation method of m and n is shown in Eq. (8).

$$\begin{cases} m=\dfrac{\alpha(\alpha-1)\lambda_n^2}{(1-\alpha\lambda_n^2)} \\ n=\dfrac{\beta(\beta-1)\lambda_t^2}{(1-\beta\lambda_t^2)} \end{cases} \tag{8}$$

The PPR cohesive model requires the eight input parameters including fracture energy (ϕ_n & ϕ_t), strength (σ_{max} & τ_{max}), initial stiffnesses (λ_n & λ_t), and softening parameters (α & β). According to the above displacement traction function, the relationship between cohesion and displacement can be drawn as shown in Fig. 1.

It can be seen from Fig. 1 that the normal and tangential cohesions are affected by both normal and tangential displacements. Simultaneously, the cohesion can change continuously and smoothly with the

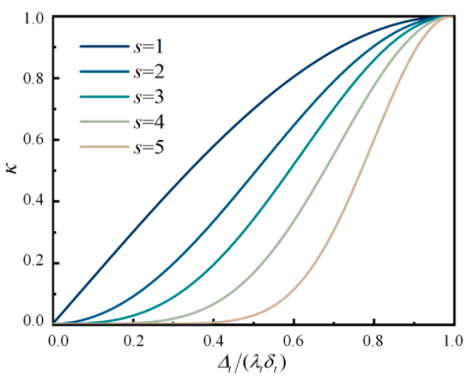

(a) Effect of the friction growth shape parameter s on the response factor κ

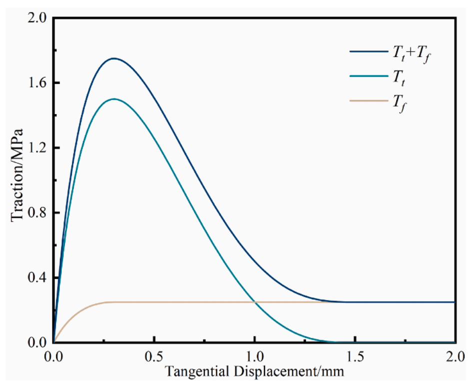

(b) Relationship between the tangential stress and the tangential displacement

Fig. 2. Coupling approach between friction and tangent traction.

normal or tangential displacement increasing.

2.2. The friction model

A new friction model coupling with the conventional PPR cohesive model is established in this section by introducing the Mohr-Coulomb strength criterion, through which the peak value of the cohesion and friction of interlayer materials can appear at the same shear deformation. The coupling relationship between friction and cohesion is controlled by Eq. (9).

$$\boldsymbol{T} = \left\{ \begin{matrix} T_n \\ T_t\frac{\Delta_2}{\Delta_t} + T_f\left(\frac{|\Delta_2|}{\Delta_t}\right)\frac{\dot{\Delta}_2}{|\dot{\Delta}_2|} \\ T_t\frac{\Delta_3}{\Delta_t} + T_f\left(\frac{|\Delta_3|}{\Delta_t}\right)\frac{\dot{\Delta}_3}{|\dot{\Delta}_3|} \end{matrix} \right\} \tag{9}$$

where T_f is the friction force; Δ_2 and Δ_3 are the relative displacements along the shear direction between the two adjacent layers, and $\Delta_t=(\Delta_2^2+\Delta_3^2)^{1/2}$; $\dot{\Delta}_2$ and $\dot{\Delta}_3$ are the related displacement increments.

When the elements on both sides of the interface are squeezed and intrude into each other, the resistance will be activated along the interface. The magnitude of resistance depends on the depth of element intrusion and the normal stiffness of the interface under compression. The normal stiffness under compression is equal to the normal stiffness when the tensile displacement approaches 0. For the proposed model, it is assumed that friction will occur when the interface is compressed, and shear slip happens between the adjacent layers. Then, it will increase smoothly with the growth of shear displacement. This process can be described by Eq. (10).

$$T_f = \boldsymbol{\mu} \times \boldsymbol{\kappa}(\Delta_t) \times |T_n|, T_n < 0 \textit{ and } \Delta_t > 0 \tag{10}$$

where μ is the interlayer friction coefficient; κ is the response factor that increases monotonically and continuously from 0 to 1 with the growth of shear displacement, and it can be expressed as follows:

$$\boldsymbol{\kappa}(\boldsymbol{\Delta}_t) = \begin{cases} \left(\frac{\boldsymbol{T}_t(\boldsymbol{0},\boldsymbol{\Delta}_t)}{\boldsymbol{\tau}_{max}}\right)^s, \boldsymbol{0} < \boldsymbol{\Delta}_t \le \lambda_t\boldsymbol{\delta}_t \\ 1, \boldsymbol{\Delta}_t > \lambda_t\boldsymbol{\delta}_t \end{cases} \tag{11}$$

where s is the transformation shape parameter controlling the growth mode of friction, and the influence of s on κ can be seen in Fig. 2**a**. Through the established friction mode, the peak cohesion and friction can appear at the same shear deformation, and the smooth transformation between cohesion and friction can be realized. Besides, $T_t(0,\Delta_t)$ represents the tangential cohesion when the normal displacement equals 0 and can be expressed by Eq. (12).

$$\boldsymbol{T}_t(\boldsymbol{0},\boldsymbol{\Delta}_t) = \frac{\boldsymbol{\Gamma}_t}{\boldsymbol{\delta}_t}\left[\boldsymbol{n}\left(1-\frac{|\boldsymbol{\Delta}_t|}{\boldsymbol{\delta}_t}\right)^{\beta}\left(\frac{\boldsymbol{n}}{\boldsymbol{\beta}}+\frac{|\boldsymbol{\Delta}_t|}{\boldsymbol{\delta}_t}\right)^{n-1} - \beta\left(1-\frac{|\boldsymbol{\Delta}_t|}{\boldsymbol{\delta}_t}\right)^{\beta-1}\left(\frac{\boldsymbol{n}}{\boldsymbol{\beta}}+\frac{|\boldsymbol{\Delta}_t|}{\boldsymbol{\delta}_t}\right)^{n}\right] \times \left[\Gamma_n\left(\frac{m}{\alpha}\right)^m + \langle\phi_n-\phi_t\rangle\right]\frac{\boldsymbol{\Delta}_t}{|\boldsymbol{\Delta}_t|} \tag{12}$$

For the proposed model, eight input parameters are required, *i.e.*, Γ_n, Γ_t, σ_{max}, τ_{max}, λ_n, λ_t, α and β. Meanshile, the friction growth shape parameter s and the friction coefficient μ should also be inputted. The curve shape of the coupled cohesion-friction model is shown in Fig. 2, and the coupling relationship between friction and tangent traction along the Δ_2 and Δ_3 directions can be expressed in Fig. 3.

In recent years, some researchers (Spring and Paulino 2015; Li et al. 2017; Baek and Park 2018) have successively proposed the coupled cohesion-friction models in the context of the PPR model. In these models, different approaches were employed to describe the friction. The comparison of the traction-displacement relationships of the proposed model in this study and the pre-existing models is illustrated in Fig. 4.

Fig. 4 shows the traction-displacement patterns of the proposed model in this study and three pre-existing models. Baek and Park (2018) assumed that friction reaches its maximum value at the onset of tangential displacement, and the friction remains constant if the normal state keeps unchanged. To accommodate this characteristic, they simplified the PPR cohesive model by setting the traction in the PPR model to reach its peak when the tangential displacement is zero, eliminating the ascending portion of the model. Their model may perform well in simulating dynamic problems dominated by friction. However, the adopted assumptions will adversely affect the convergence of numerical calculations for some quasi-static problems. Meanwhile, when modelling the interface mechanical behavior with initial low stiffness, this model may impart excessively high elastic stiffness to the interface. By contrast, Spring and Paulino (2015) did not modify the original PPR cohesive model. Instead, they introduced a κ-factor to describe the variation of frictional force with the relative displacement of interface and assumed that this factor remains 0 until the traction reaches its peak. These treatments can lead to a phase shift between traction and friction. However, when fitting shear strength and friction coefficient, it is not straightforward to deconstruct the actual interface strength into the sum of friction and cohesion. Besides, in the model proposed by Li et al. (2017), the relationship between the peak shear displacement and the cohesion is uncertain. Simultaneously, their model did not consider that both cohesive and frictional terms are continuously differentiable with respect to tangential displacement. Actually, Park et al. (2009) pointed out that the continuous differentiability of the traction-displacement equation can significantly improve the numerical

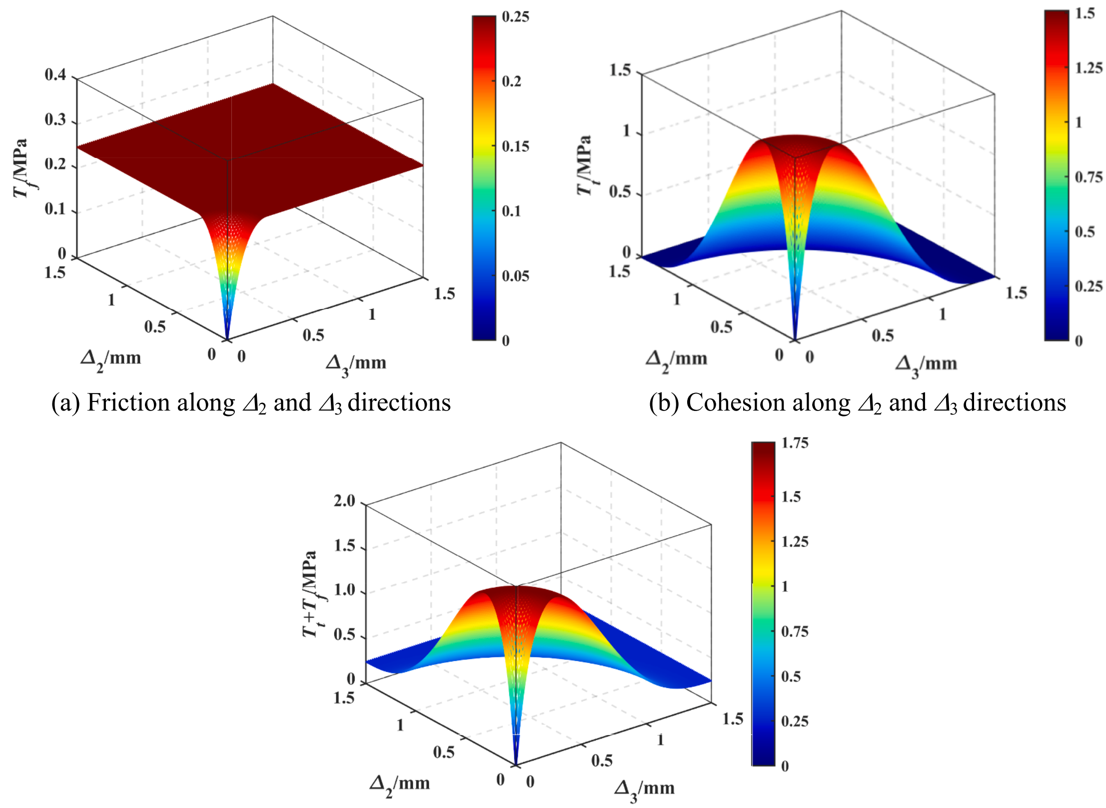

(a) Friction along Δ_2 and Δ_3 directions

(b) Cohesion along Δ_2 and Δ_3 directions

(c) Coupled friction and cohesion along Δ_2 and Δ_3 directions

Fig. 3. Interactive Influence of friction and cohesion.

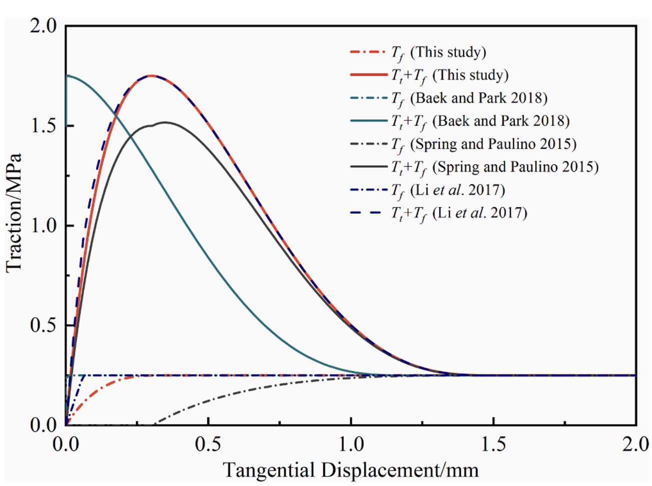

Fig. 4. Comparison of the traction-displacement patterns of different models.

convergence. Note that the proposed model in this study can ensure the continuous differentiability of the traction-displacement governing equation and precisely provide shear strength through the combined contribution of friction and cohesion. Additionally, by taking the non-negligible initial stiffness of the interface into account, the proposed model can effectively characterize the deformation behavior of interface under relatively low stiffness at the initial stage of loading.

Simultaneously, the tangent stiffness matrix (***D***) of materials should be determined, and its matrix form is shown in Eq. (13). The tangent stiffness of materials along each direction can be obtained by solving the second-order differential equation of the potential energy function. In our model, the calculation method for the material stiffness matrix can be expressed by Eq. (14) according to Spring and Paulino (2015), Park and Paulino (2012) and Spring and Paulino (2014).

$$\boldsymbol{D} = \begin{bmatrix} D_{11} & D_{12} & D_{13} \\ D_{21} & D_{22} & D_{23} \\ D_{31} & D_{32} & D_{33} \end{bmatrix} \tag{13}$$

$$D_{11} = \frac{\partial T_n}{\partial \Delta_n} D_{12} = \frac{\partial T_n}{\partial \Delta_t}\frac{\Delta_2}{\Delta_t}$$

$$D_{13} = \frac{\partial T_n}{\partial \Delta_t}\frac{\Delta_3}{\Delta_t} \tag{14}$$

$$D_{21} = \frac{\partial T_t}{\partial \Delta_n}$$

$$\frac{\Delta_2}{\Delta_t} + \frac{\partial T_f}{\partial \Delta_n}\frac{|\Delta_2|}{\Delta_t}\frac{\dot{\Delta}_2}{\left|\dot{\Delta}_2\right|}$$

$$D_{22} = \left(\frac{\partial T_t}{\partial \Delta_t}\Delta_2 + \frac{\partial T_f}{\partial \Delta_t}|\Delta_2|\frac{\dot{\Delta}_2}{\left|\dot{\Delta}_2\right|}\right)$$

$$\frac{\Delta_2}{\Delta_t^2} - \left(T_t + T_f\frac{\Delta_2}{|\Delta_2|}\frac{\dot{\Delta}_2}{\left|\dot{\Delta}_2\right|}\right)$$

$$\frac{\Delta_3^2}{\Delta_t^3}$$

$$D_{23} = \left(\frac{\partial T_t}{\partial \Delta_t}\Delta_2 + \frac{\partial T_f}{\partial \Delta_t}|\Delta_2|\frac{\dot{\Delta}_2}{\left|\dot{\Delta}_2\right|}\right)\frac{\Delta_3}{\Delta_t^2} - \left(T_t\Delta_2 + T_f|\Delta_2|\frac{\dot{\Delta}_2}{\left|\dot{\Delta}_2\right|}\right)\frac{\Delta_3}{\Delta_t^3}$$

$$D_{31} = \frac{\partial T_t}{\partial \Delta_n}\frac{\Delta_3}{\Delta_t} + \frac{\partial T_f}{\partial \Delta_n}\frac{|\Delta_3|}{\Delta_t}\frac{\dot{\Delta}_3}{\left|\dot{\Delta}_3\right|}$$

$$D_{32} = \left(\frac{\partial T_t}{\partial \Delta_t}\Delta_3 + \frac{\partial T_f}{\partial \Delta_t}|\Delta_3|\frac{\dot{\Delta}_3}{\left|\dot{\Delta}_3\right|}\right)\frac{\Delta_2}{\Delta_t^2} - \left(T_t\Delta_3 + T_f|\Delta_3|\frac{\dot{\Delta}_3}{\left|\dot{\Delta}_3\right|}\right)\frac{\Delta_3}{\Delta_t^3}$$

$$D_{33} = \left(\frac{\partial T_t}{\partial \Delta_t}\Delta_3 + \frac{\partial T_f}{\partial \Delta_t}|\Delta_3|\frac{\dot{\Delta}_3}{\left|\dot{\Delta}_3\right|}\right)\frac{\Delta_3}{\Delta_t^2} - \left(T_t + T_f\frac{\Delta_3}{|\Delta_3|}\frac{\dot{\Delta}_3}{\left|\dot{\Delta}_3\right|}\right)\frac{\Delta_2}{\Delta_t^3}$$

where the expressions of $\frac{\partial T_n}{\partial \Delta_n}, \frac{\partial T_n}{\partial \Delta_t}, \frac{\partial T_t}{\partial \Delta_n}$ and $\frac{\partial T_t}{\partial \Delta_t}$ are given by Eq. (15).

$$\begin{aligned}
\frac{\partial T_n}{\partial \Delta_n} = {} & \frac{\Gamma_n}{\delta_n^2}\left[\left(m^2-m\right)\left(1-\frac{\Delta_n}{\delta_n}\right)^{\alpha}\left(\frac{m}{\alpha}+\frac{\Delta_n}{\delta_n}\right)^{m-2}\right. \\
& + \left(\alpha^2-\alpha\right)\left(1-\frac{\Delta_n}{\delta_n}\right)^{\alpha-2}\left(\frac{m}{\alpha}+\frac{\Delta_n}{\delta_n}\right)^{m} \\
& \left. - 2\alpha m\left(1-\frac{\Delta_n}{\delta_n}\right)^{\alpha-1}\left(\frac{m}{\alpha}+\frac{\Delta_n}{\delta_n}\right)^{m-1}\right] \times \left[\Gamma_t\left(1-\frac{|\Delta_t|}{\delta_t}\right)^{\beta}\left(\frac{n}{\beta}+\frac{|\Delta_t|}{\delta_t}\right)^{n}\right. \\
& \left. + \langle\phi_t-\phi_n\rangle\right]\frac{\partial T_t}{\partial \Delta_t} \\
= {} & \frac{\Gamma_t}{\delta_t^2}\left[\left(n^2-n\right)\left(1-\frac{|\Delta_t|}{\delta_t}\right)^{\beta}\left(\frac{n}{\beta}+\frac{|\Delta_t|}{\delta_t}\right)^{n-2}\right. \\
& + \left(\beta^2-\beta\right)\left(1-\frac{\Delta_n}{\delta_n}\right)^{\beta-2}\left(\frac{n}{\beta}+\frac{|\Delta_t|}{\delta_t}\right)^{n} \\
& \left. - 2\beta n\left(1-\frac{|\Delta_t|}{\delta_t}\right)^{\beta-1}\left(\frac{n}{\beta}+\frac{|\Delta_t|}{\delta_t}\right)^{n-1}\right]\left[\Gamma_n\left(1-\frac{\Delta_n}{\delta_n}\right)^{\alpha}\left(\frac{m}{\alpha}+\frac{\Delta_n}{\delta_n}\right)^{m}\right. \\
& \left. + \langle\phi_n-\phi_t\rangle\right]\frac{\partial T_n}{\partial \Delta_t} \\
= {} & \frac{\Gamma_n\Gamma_t}{\delta_n\delta_t}\left[m\left(1-\frac{\Delta_n}{\delta_n}\right)^{\alpha}\left(\frac{m}{\alpha}+\frac{\Delta_n}{\delta_n}\right)^{m-1} - \alpha\left(1-\frac{\Delta_n}{\delta_n}\right)^{\alpha-1}\left(\frac{m}{\alpha}+\frac{\Delta_n}{\delta_n}\right)^{m}\right] \\
& \times\left[n\left(1-\frac{|\Delta_t|}{\delta_t}\right)^{\beta}\left(\frac{n}{\beta}+\frac{|\Delta_t|}{\delta_t}\right)^{n-1}\right. \\
& \left. - \beta\left(1-\frac{|\Delta_t|}{\delta_t}\right)^{\beta-1}\left(\frac{n}{\beta}+\frac{|\Delta_t|}{\delta_t}\right)^{n}\right]\frac{\Delta_t}{|\Delta_t|}\frac{\partial T_t}{\partial \Delta_n} \\
= {} & \frac{\partial T_n}{\partial \Delta_t}
\end{aligned}$$

(15)

The expressions of $\frac{\partial T_f}{\partial \Delta_n}$ and $\frac{\partial T_f}{\partial \Delta_t}$ are given by Eq. (16).

$$\begin{aligned}
\frac{\partial T_f}{\partial \Delta_t} &= s\mu\left(\frac{T_t(0,\Delta_t)}{\tau_{\max}}\right)^{s-1}\frac{\partial T_t}{\partial \Delta_t}|T_n| \\
\frac{\partial T_f}{\partial \Delta_n} &= \mu\left(\frac{T(0,\Delta_t)}{\tau_{\max}}\right)^{s}\frac{T_n}{|T_n|}\left|\frac{\partial T_n}{\partial \Delta_n}\right|
\end{aligned} \tag{16}$$

2.3. The unloading and reloading relation

In practical cases, the loading on composite structures is not monotonous, which means that unloading and reloading may occur. In order to predict the stress and deformation characteristics of composite structures appropriately, the unloading and reloading has been achieved in our model by referring to Park and Paulino (2012), Li et al. (2017) and Baek and Park (2018). During unloading and reloading, the fracture energy can also vary accordingly. The unloading and reloading curves are closely related to the original loading curve and can be expressed by Eq. (17).

$$\begin{aligned}
T_n^v(\Delta_n,\Delta_t) &= T_n(\Delta_{n_{\max}},\Delta_t)\left(\frac{\Delta_n}{\Delta_{n_{\max}}}\right)^{\alpha_v} \\
T_t^v(\Delta_n,\Delta_t) &= T_t(\Delta_n,\Delta_{t_{\max}})\left(\frac{|\Delta_t|}{\Delta_{t_{\max}}}\right)^{\beta_v}\frac{\Delta_t}{|\Delta_t|}
\end{aligned} \tag{17}$$

where α_v and β_v are the parameters controlling the shape of the unloading and reloading traction curves. Generally, both are taken as 1, meaning that the linear curve is adopted; $\Delta_{n_{\max}}$ and $\Delta_{t_{\max}}$ are the maximum relative displacements along the normal and tangential directions during the loading history. Therefore, from Eq. (17), it can be found that T_n^v and T_t^v depend on the loading history. In addition, in terms of the tangential behavior, the friction direction during unloading will be opposite to the original direction. Thus, in this case, the $T_t + T_f$ curve will be adjusted quickly with the jump amplitude of 2×abs(T_f), as shown in Fig. 5.

Fig. 5 shows the loading and unloading relationship of the proposed coupled model. Note that when the shear direction changes, the magnitude of the friction will remain constant, but the direction will reverse. Therefore, when the normal state keeps unchanged, the friction will jump with a amplitude of abs(T_f-($-T_f$))=2×abs(T_f). This approach can also be found in the studies by Li et al. (2017) and Baek and Park (2018). When entering the softening stage, the tangent stiffness of the unloading and reloading relationship curve is different from the monotonic loading, and it can be expressed as follows:

$$\begin{aligned}
\frac{\partial T_n^v}{\partial \Delta_n} &= T_n(\Delta_{n_{\max}},\Delta_t)\frac{\alpha_v}{\Delta_{n_{\max}}}\left(\frac{\Delta_n}{\Delta_{n_{\max}}}\right)^{\alpha_v-1} \\
\frac{\partial T_n^v}{\partial \Delta_t} &= \frac{\partial T_n(\Delta_{n_{\max}},\Delta_t)}{\partial \Delta_t}\left(\frac{\Delta_n}{\Delta_{n_{\max}}}\right)^{\alpha_v} \\
\frac{\partial T_t^v}{\partial \Delta_n} &= \frac{\partial T_t(\Delta_n,\Delta_{t_{\max}})}{\partial \Delta_n}\left(\frac{|\Delta_t|}{\Delta_{t_{\max}}}\right)^{\beta_v} \\
\frac{\partial T_t^v}{\partial \Delta_t} &= T_t(\Delta_n,\Delta_{t_{\max}})\frac{\beta_v}{\Delta_{t_{\max}}}\left(\frac{|\Delta_t|}{\Delta_{t_{\max}}}\right)^{\beta_v-1}
\end{aligned} \tag{18}$$

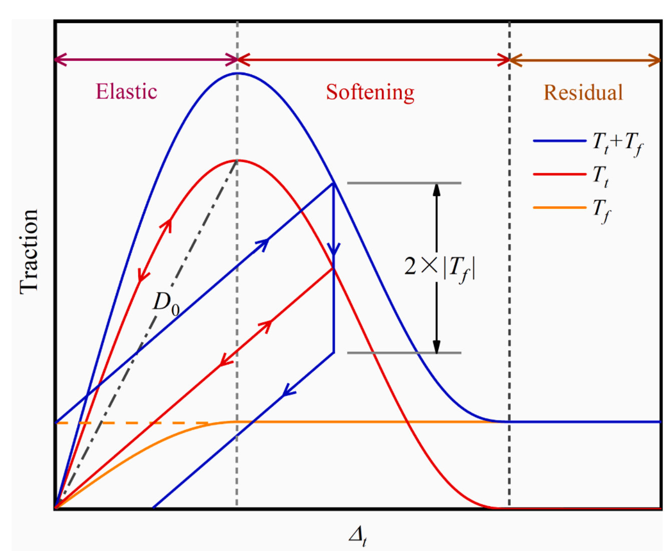

Fig. 5. Unloading and reloading relation of cohesion and friction model.

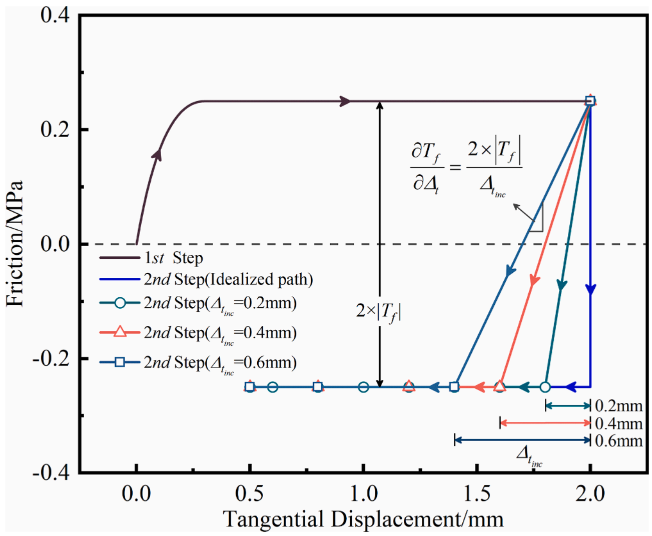

Fig. 6. The variation and tangential stiffness of friction term during shearing.

To ensure the convergence of the numerical calculation, when the unloading and reloading behavior is deactivated, the contents of $\frac{\partial T_n}{\partial \Delta_n}$, $\frac{\partial T_n}{\partial \Delta_t}$, $\frac{\partial T_t}{\partial \Delta_n}$ and $\frac{\partial T_t}{\partial \Delta_t}$ in the tangent stiffness matrix will be updated according to Eq. (14). However, once the unloading and reloading behavior is activated, they will be updated according to Eq. (18).

It is worth noting that when the direction of tangential separation changes, friction also varies accordingly. For numerical calculation, the ideal vertical drop would hinder numerical convergence. Hence, incremental time steps are adopted to solve this problem. Clearly, when the change of the direction of shear slip is detected, the developed model will consider the effect of friction jump on the governing equations by updating the tangential stiffness of friction term. The relative slip deformation along the tangential axis can be determined as $\Delta_{t_{inc}}$. Then, the ratio of the required jump magnitude to the relative tangential deformation can be defined as the tangential stiffness of friction term at current increment step. At an increment step when the direction of shear changes, there will inevitably be a shear slip deformation. Therefore, the tangential stiffnesses of both friction and cohesive terms contribute to the global tangential matrix. This established procedure ensures the numerical convergence of the developed model. At a certain increment step, the tangential stiffness caused by friction jump can be determined using Eq. (19).

$$\frac{\partial T_f}{\partial \Delta_t} = \frac{2 \times |T_f|}{\Delta_{t_{inc}}} \tag{19}$$

where $\Delta_{t_{inc}}$ is the shear slip deformation at an interface.

To illustrate the numerical process of friction, two blocks on both sides of an interface are treated to be rigid to ensure that the applied shear displacement is equal to the relative slip along the cohesive interface. Then, the shear displacement applied on the blocks increases from 0 mm to 2 mm during the first analysis step and decreased from 2 mm to 0.5 mm. during the second analysis step. The friction vs. tangential displacement curves obtained using various increments, *i.e.*, 0.2 mm, 0.4 mm and 0.6 mm are shown in Fig. 6.

From Fig. 6, it can been seen that when the tangential slip direction is reversed, the friction jump differs from the ideal vertical drop. Actually, a finite slope is adopted according to the increment of reverse slip along the interface, and the friction jump is completed at the end of the increment step. Furthermore, the tangential stiffness of friction term is calculate based on the slip increment. To intuitively display the established reloading and unloading mode, a numerical shear model with the geometry shown in Fig. 7 is tested.

Firstly, the numerical model is loaded with two different vertical displacements (U_1) on the top surface, *i.e.*, U_{1a}=0.0mm, U_{1b}=-0.5mm. Then, the deformation characteristics under unloading and reloading with and without friction are simulated and compared. The total time of the steps is 1.3s, and the amplitudes of U_{1a}, U_{1b} and U_2 are shown in Fig. 8.

The upper and lower parts are both elastic. The elastic modulus and Poisson's ratio of the upper part is 1,200 MPa and 0.3. Meanwhile, the elastic modulus and Poisson's ratio of the lower part is 1,500 MPa and 0.25. The parameters of the interlayer are σ_{max}=0.075 MPa, τ_{max}=0.075

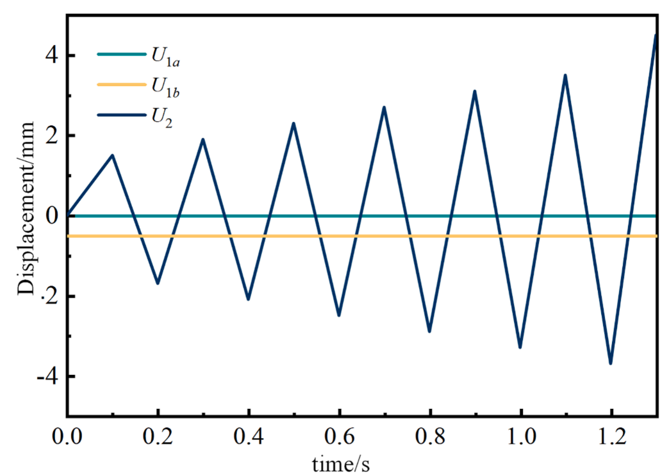

Fig. 8. The amplitudes of U_{1a}, U_{1b} and U_2.

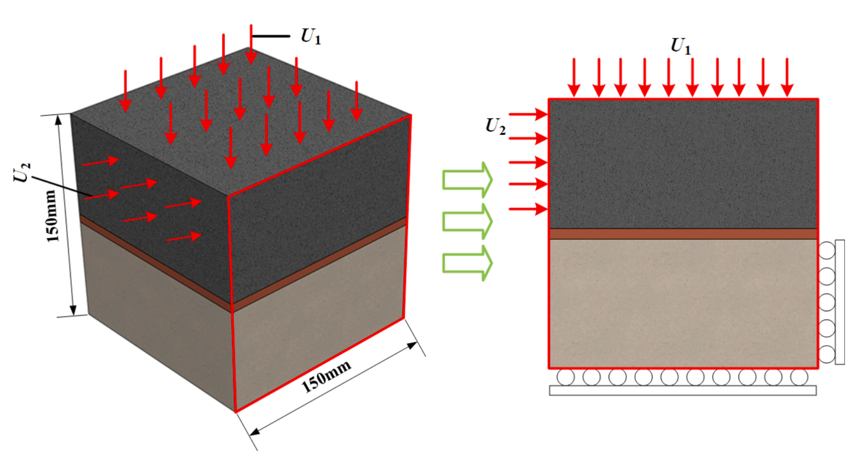

Fig. 7. Model for the direct shear test.

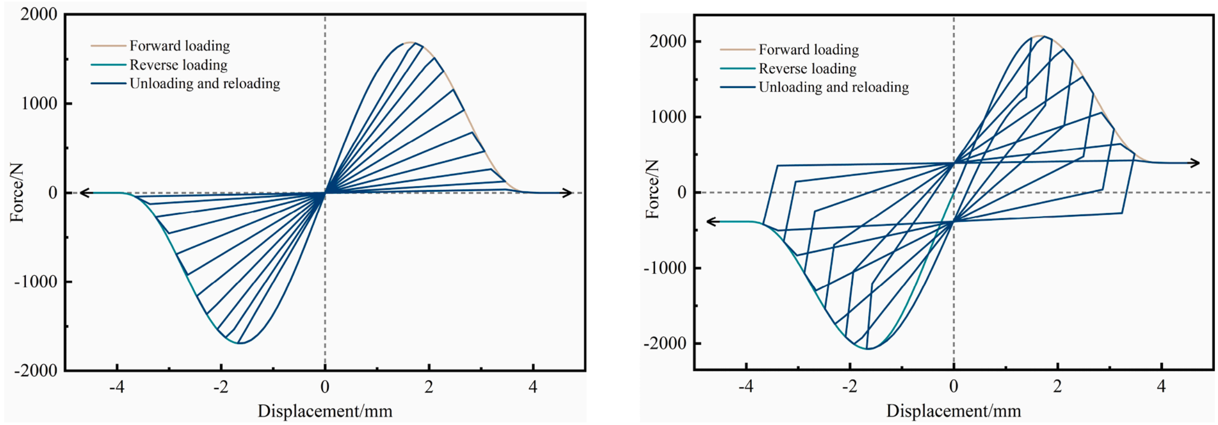

(a) U_{1a} **(b)** U_{1b}

Fig. 9. The displacement-force curve of the shear test model.

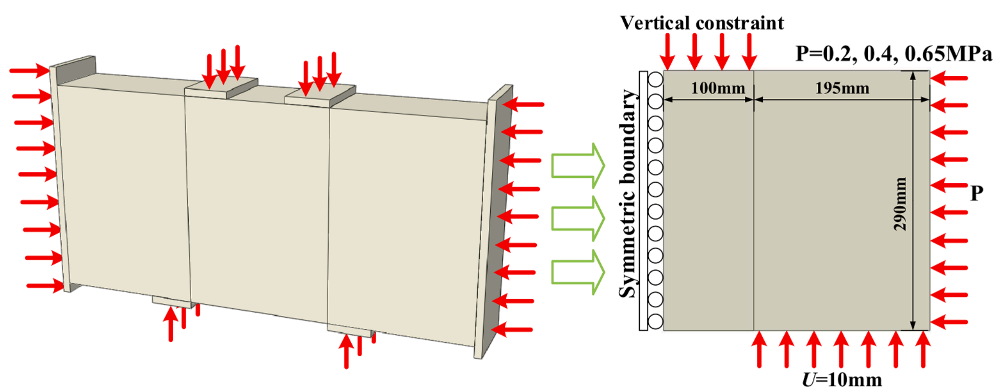

(a) Experiment model (Beyer *et al.* 2010, 2012) **(b) Numerical model**

Fig. 10. Numerical verification of masonry wallette.

MPa, f_n=0.16 MPa•mm, f_n=0.16 MPa•mm, α=4, β=4, λ_n=0.4, λ_t=0.4, s=1.7 and μ=0.504. The obtained results of shear displacement amplitude and reaction force of the two preset conditions are extracted, and the simulated displacement-force curves are shown in Fig. 9.

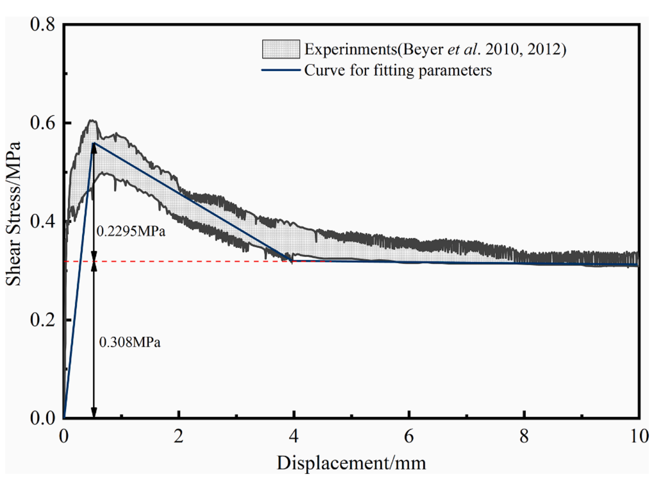

Fig. 11. The parameter fitting using the experimental data.

3. Numerical benchmark and application

3.1. Shear test of the masonry wallette

Masonry wallette is wildly used in civil engineering. The experiment conducted by Beyer et al. (2010, 2012) on the Masonry wallette is chosen to verify the correctness and effectiveness of the proposed cohesion-friction mode. As shown in Fig. 10**a**, there are three bricks bonded by mortar, the middle brick is also constrained by two rigid bricks on the upper surface. Besides, the bilateral bricks are applied with the vertical displacement load on the lower surfaces to achieve shear effect. A pressure is applied onto the two outer vertical surfaces to ensure the friction effect.

Table 1
Material parameters of bricks and joint mortar used in numerical simulation.

Parameter	Value
Mode I fracture energy ϕ_n/MPa•mm	0.125
Mode II fracture energy ϕ_n/MPa•mm	0.45
Normal cohesive strength σ_{max}/MPa	0.2295
Tangential cohesive strength τ_{max}/MPa	0.2295
Normal initial slope indicator λ_n	0.06
Tangential initial slope indicator λ_t	0.06
Normal shape parameter α	5.0
Tangential shape parameter β	5.0
Friction shape parameter s	1.0
Friction Coefficifient μ	0.77

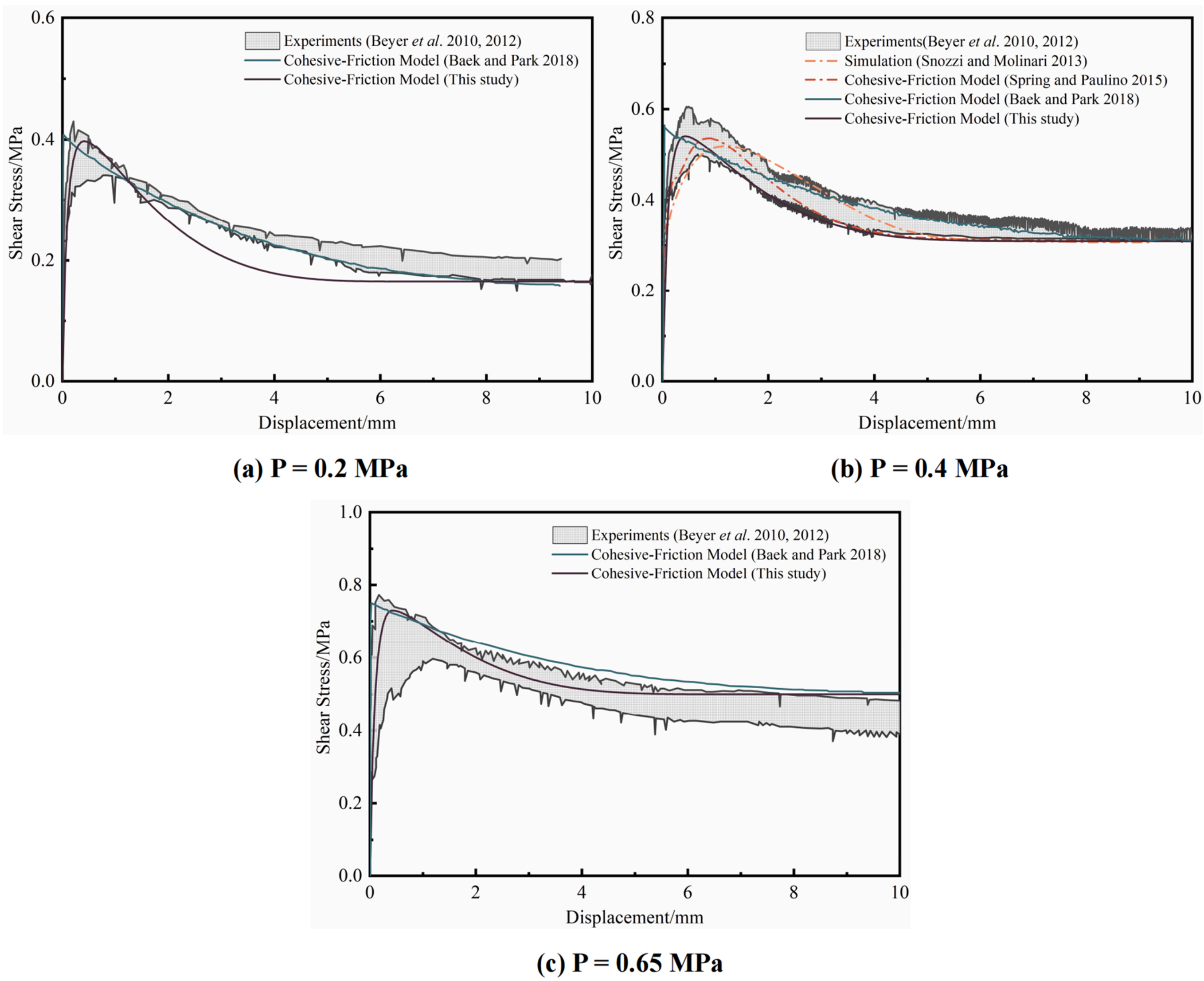

Fig. 12. Shear stress vs. applied displacement curves of the masonry wallette.

In the experiment by Beyer et al. (2010, 2012), the pressures of 0.2 MPa, 0.4 MPa, and 0.65 MPa were applied. This experiment has also been simulated using different numerical models (Spring and Paulino 2015; Snozzi and Molinari 2013; Baek and Park 2018). Considering that the symmetric half model was used by Spring and Paulino (2015), Snozzi and Molinari (2013) and Baek and Park (2018) as shown in Fig. 10**b,** such model is also used in this section for strict comparison purpose. Firstly, the normal pressure is applied on the right surface of the specimen and keeps constant during the shearing. Then, a vertical displacement of 10 mm is loaded on the lower surface of the right brick. Simultaneously, a vertical constrain is applied on the upper surface of light brick. Therefore, the joint interface is in the compress-shear state during the loading. The static solving algorithm is adopted, and the total time of shear load steps can be set as 1s because of the time independence of the algorithm. The three-dimensional (3D) eight-nodes linear elements are selected to discretize the bricks, and the eight-nodes cohesive elements are inserted into the joint region between the bricks. In the numerical studies by Spring and Paulino (2015) and Snozzi and Molinari (2013), they chose the pressure of 0.4 MPa for calibration. Baek and Park (2018) chose the pressure of 0.2 MPa, 0.4 MPa, 0.65 MPa. In this study, the fitting parameters are determined when the pressure is 0.4 MPa. However, the other normal pressures are also simulated for the comprehensive validation as shown in Fig. 11.

According to the Mohr-Coulomb strength criterion, the peak shear stress can be divided into two parts. The first part is contributed by the cohesion, which is approximately 0.2295 MPa; the other part is contributed by the friction, which is about 0.308 MPa. Because the normal pressure of 0.4 MPa is applied, it can be deduced that the friction coefficient is 0.77. The other parameters are determined by fitting the shape of the oscillating area in Fig. 11 through the trial and error process. The material parameters of bricks and joint mortar are shown in Table 1. Additionally, it is assumed that the brick is linear elastic with the elastic modulus of 14,000 MPa and Poisson's ratio of 0.15.

The shear stress vs. displacement curves predicted by the different models are compared with the experimental data (Beyer et al. 2010, 2012) as shown in Fig. 12. It shows that the proposed model in this study can effectively simulate the shear slip behavior of bricks under different normal pressures. The simulated curves are basically covered by the envelope of the experimental data. Furthermore, the displacement corresponding to the peak shear stress is nearly identical to the experimental value, and the residual stress also falls within the envelope of the experimental results. In the case of 0.2 MPa pressure, the softening stage computed by the proposed model differs from the physical test because the material parameters are determined by fiting the experimental data when the pressure is 0.4 MPa. When the pressure equals 0.4 MPa, the predicted curve by the proposed model agrees with the experiment with

Table 2
The critical indices of each model and their relative errors.

Experiment/ Model	Beyer and Dazio (2012)	Snozzi and Molinari (2013)	Spring and Paulino (2015)	Baek and Park (2018)	This study
Peak shear stress/ MPa	0.550	0.519	0.536	0.562	0.540
Relative error/%	–	5.64	2.55	2.18	1.82
Displacement at peak shear stress/mm	0.496	1.259	0.898	0.044	0.422
Relative error/%	–	153.83	81.05	91.13	14.92
Initial displacement at residual stage/ mm	5.888	5.591	5.591	8.772	5.591
Relative error/%	–	5.04	5.04	48.98	5.04
Tangential cohesive strength/MPa	0.25	0.3	0.45	0.25	0.229
Relative error/%	–	20.00	80.00	0.00	8.40
Friction coefficient	0.77	0.77	0.77	0.77	0.77
Relative error/%	–	0	0	0	0

Notes: The peak shear stress reported by Beyer and Dazio (2012) fluctuates within a certain range. Therefore, the average value is chosen. Meanwhile, the highest point of the fluctuation range is used to determine the displacement value corresponding to the peak shear stress.

satisfactory accuracy. Besides, the calculated peak shear stress, the displacement corresponding to peak shear stress, the initial displacement at residual stage, the tangential cohesive strength, the friction coefficient and their relative errors are listed in Table 2.

From Table 2, it can be seen that the relative errors of the proposed model and the pre-existing models (Snozzi and Molinari 2013; Spring and Paulino 2015; Baek and Park 2018) are 14.92%, 153.83%, 81.05%, 91.13%, respectively when calculating the displacement corresponding to peak shear stress. In terms of peak shear stress and initial displacement at residual stage, the performance of the proposed model is also the best. Although for tangential cohesive strength, the relative error of the proposed model is larger than the model developed by Baek and Park (2018), it is still much smaller than the other two models. The satisfactory accuracy produced by the proposed model is mainly because the shear strength and friction coefficient obtained from the physical experiment can be applied directly. Simultaneously, the ultimate failure displacement can also be directly determined based on the experimental data, meaning that the tangential initial slope indicator λ_t can be determined in a straightforward manner. Moreover, from Fig. 12, it can be seen that the peak shear stress of the proposed model occurs at a small displacement. This is because the peaks of friction and cohesive are set to be synchronous, facilitating the effective control of the peaks and their corresponding displacements during the parameter fitting. Besides, when the peak shear stress is reached, the predicted curve of the proposed model exhibits a steep slope downward and approaches the lower bound of the experimental results thereafter. This phenomenon is mainly because the shear-fracture-induced energy is calculated using a triangular area whose base and height are equal to the ultimate failure displacement and the shear strength, respectively. Hence, the accuracy can be further improved by calculating the released energy precisely. However, more detailed experimental data are therefore necessary. It is worth noting that the material parameters including the peak stress, tangential cohesive strength and residual stress are determined by fitting the experimental data under 0.4 MPa pressure as shown in Fig. 11. The curve comparison in Fig. 12 and the error analysis in Table 2 confirm the effectiveness of the proposed model.

3.2. Eccentric compression test of the circular concrete-filled steel tube

In this section, the effects of the coronal gap height and the angle between loading direction and coronal gap axis on the bending and bearing capacity of CCFST under eccentric compression are investigated. In actual engineering projects, the CCFST structures may suffer eccentric compression due to inaccurate construction or changes of external loads. In the following simulation, the eccentric distance is set to be 20 mm, and two monitoring points are assigned on the top and bottom sections of CCFST. The displacement-control vertical loading is applied at the top loading point which is 20 mm away from the center point of the top section until the final instability of the CCFST. Besides, the configuration of the angle between cap gap axis and loading direction is defined as shown Fig. 13. With the aim of systematically revealing the effect of loading angle, the loading angle changes from 0° to 180° with an interval of 3°. Meanwhile, the coronal gap height is set to be 0 mm, 2.5 mm, 5.0 mm and 7.5 mm, respectively. The model geometry is shown in Fig. 14.

In the numerical model of CCFST, the concrete core is simulated by the 3D 8-node reduced integral elements. The outer steel tube is simulated by the 4-node reduced integral shell element. Meanwhile, the concrete damage plastic constitutive model is adopted (Hillerborg et al. 1976; Lee and Fenves 1998; Lubliner et al. 1989), and the stress–strain relationship refers to the previous studies (Mander and Priestley 1988a; Mander and Priestley, 1988b; Han and An 2014). As a simplification, the ideal bilinear elastoplastic model (Kabir et al. 2019) is applied with the elastic modulus of 2.1×10^5 MPa, the Poisson's ratio of 0.3, and the yield stress of 335 MPa. Besides, the cement mortar interlayer is simulated by

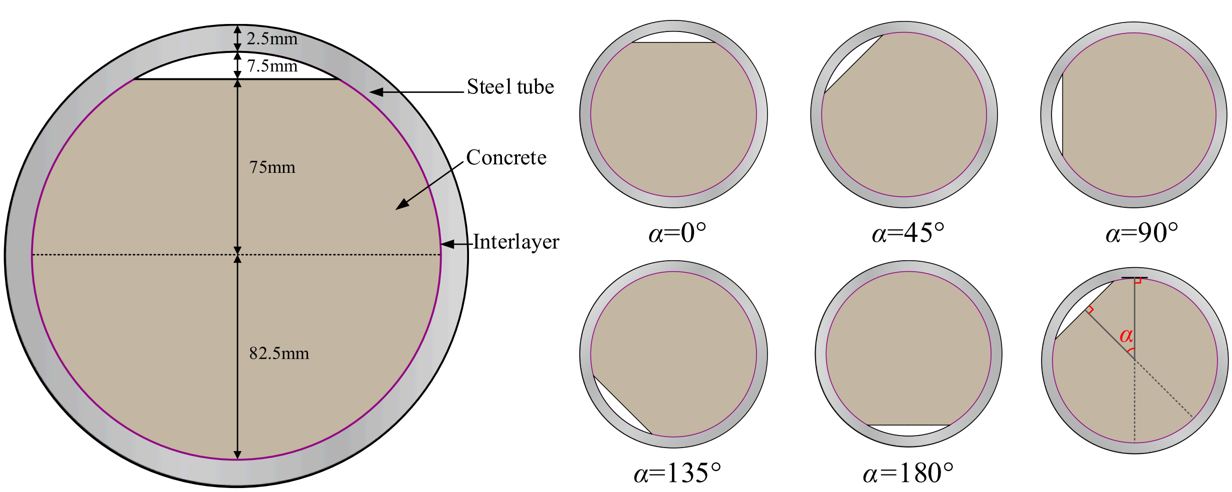

Fig. 13. Changes of the angle between load direction and coronal gap axis.

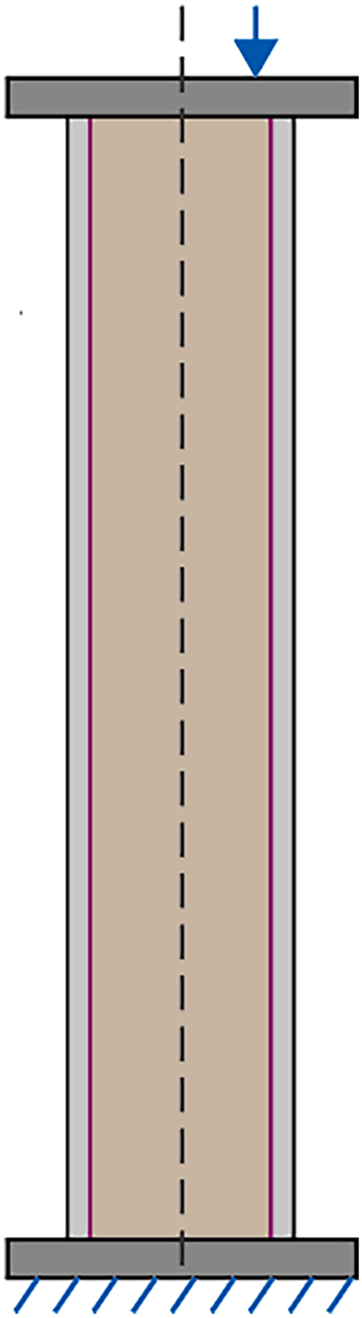

Fig. 14. Eccentric compression setting of CCFST.

the cohesive elements. The Mode I and Mode II fracture energy of mortar interlayer are determined according to Nasiri and Liu (2017), and the initial stiffness and strength are derived by the test data (Tao et al. 2016). The friction coefficient is set as 0.6 (Wang et al. 2013). The material properties are shown in Table 3.

Fig. 15 illustrates the calculated force–displacement curves of the 61×4 CCFST models with different loading angles under varying coronal gap heights. Namely, for a certain coronal gap height, 61 CCFST models with the angle between loading direction and coronal gap changing from 0° to 180° by an interval of 3° are tested under eccentric compression, and 4 coronal gap heights are considered. As displays in Fig. 13, the minimum of 0 mm represents that the pouring of core concrete is perfect and there is no coronal gap defect, and the maximum of 7.5 mm means that there is a relatively large gap defect which may significantly influence the mechanical performance of the CCFST structure. From Fig. 15, we can see that the numerical results exhibit the typical softening and yield characteristics. Before the peak force, the CCFST structures displays the apparent linear-elastic behavior. However, with the gradual growth of the external loading, the bearing force increases nonlinearly when approaching the peak value. Although the average peak bearing forces almost remain at the same level for different coronal gap heights, the fluctuation ranges of the initial deformation modulus, peak bearing force and residual strength increase as the coronal gap height grows up. It means that the bearing capacity of CCFST becomes more and more sensitive to the dip angle between loading direction and coronal gap axis as the coronal gap height rises.

Table 3
The mechanical parameters of interlayer.

Parameter	Value
Mode I fracture energy ϕ_n/MPa•mm	0.04
Mode II fracture energy ϕ_n/MPa•mm	0.4
Normal cohesive strength σ_{max}/MPa	0.2
Tangential cohesive strength τ_{max}/MPa	1.0
Normal initial slope indicator λ_n	0.25
Tangential initial slope indicator λ_t	0.25
Normal shape parameter α	5.0
Tangential shape parameter β	5.0
Friction shape parameter s	4.0
Coefficient of friction μ	0.6

Fig. 16 illustrates the relationship between the eccentric compression strength and the dip angle between coronal gap axis and loading direction. The varying trend is not affected by the loading angle when there is no coronal gap, which is consist with the actual monitoring. Meanwhile, the CCFST strength keeps decreasing and becomes more and more sensitive to the change of the loading angle as the coronal gap height increases. Clearly, the fluctuation range of the CCFST strength is enlarged by the growth of the coronal gap height. However, the fluctuation shows various detailed changing trends. When the loading angle increases from 0° to 108°, the eccentric compression strength of CCFST continuously rises to the maximum value. However, it starts to drop with the loading angle keeping increasing and reaches a trough when the loading angle is 180°. Besides, the eccentric compression strength reaches the minimum value when the loading angle is 0°, and the strength-angle curves are axisymmetric for the loading angle ranges of [0°, 180°] and [180°, 360°].

The probability distribution of the calculated CCFST strengths affected by different coronal gap heights is shown in Fig. 17. Here, the bar chart displays the statistical number of the same CCFST strengths for a specific coronal gap height; the red curve represents the best multimodal fitting line of the peak strength distribution; the red dotted curve represents the cumulative occurrence frequency of a certain CCFST strength. From Fig. 17, it can be seen that the frequency distribution of the eccentric compressive strengths follows the bimodal pattern, *i.e.*, the slow growth in the early stage and the rapid growth in the late stage. Simultaneously, the two probability peaks of the possible CCFST strengths can be observed for each coronal gap height, indicating the two extremes of a CCFST structure. However, the probability of the first crest is obviously smaller than the second one. Although as a good signal for safe construction, the most proportion of CCFST eccentric compressive strengths concentrate at the high value range, there is still a large proportion occur at the low value range. This phenomenon cannot be ignored for the design and management of CCFST structures.

Fig. 18 illustrates the variation of the strength, mean strength, and covariance (COV) of the CCFST structures with varying coronal gap heights. The COV is defined as the ratio between the standard deviation and the mean of the strengths for each gap height. When the coronal gap changes from 0 mm, 2.5 mm, 5.0 mm to 7.5 mm, the COV values increases from 0, 0.0027, 0.0080 to 0.0148. It means that with the gradual growth of coronal gap height, the dispersion of the eccentric compressive strength distribution of CCFSTs becomes greater. Furthermore, the increasing amplitude of the strength distribution dispersion of also

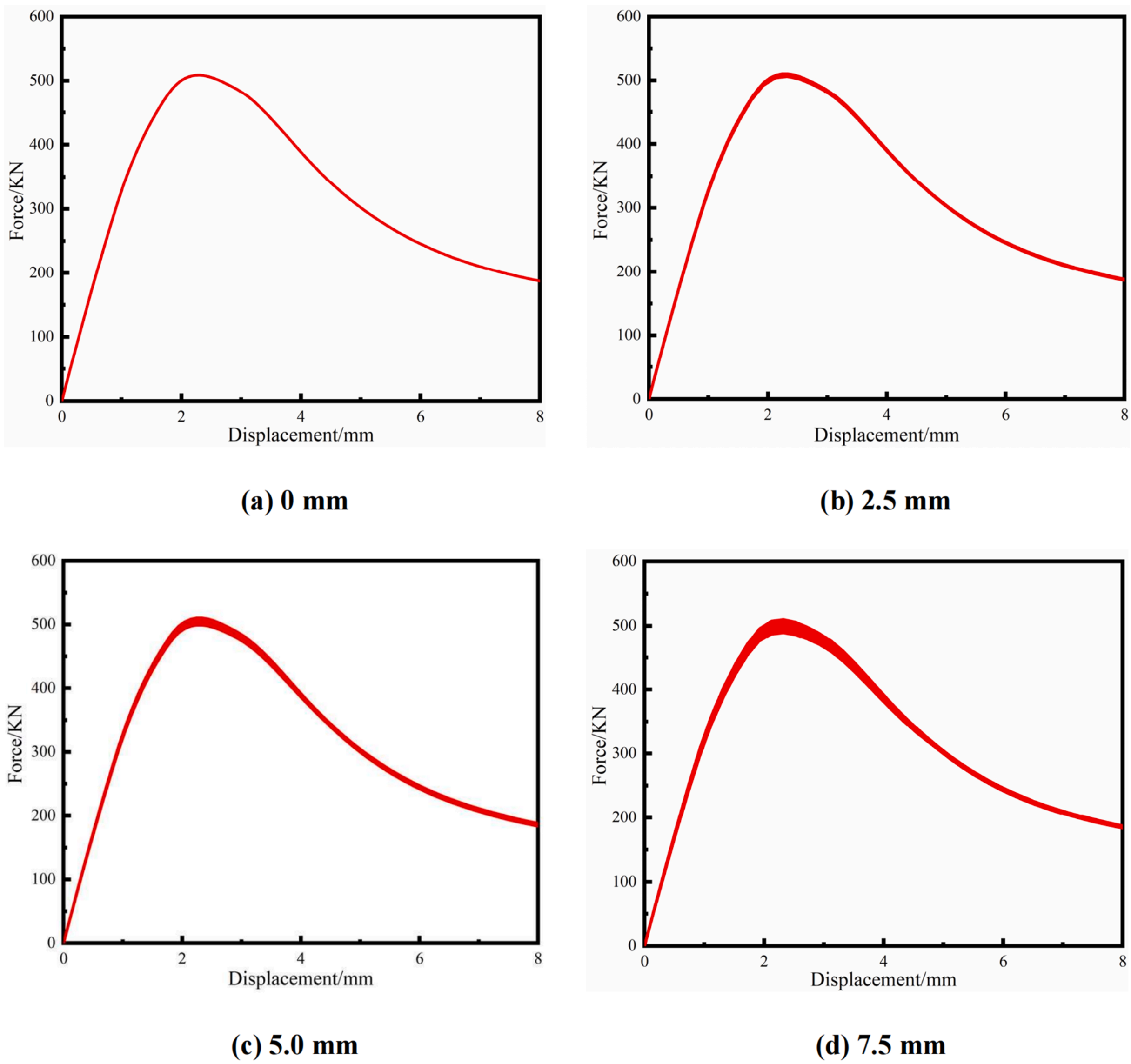

Fig. 15. The force–displacement curves of CCFST under different coronal gap heights.

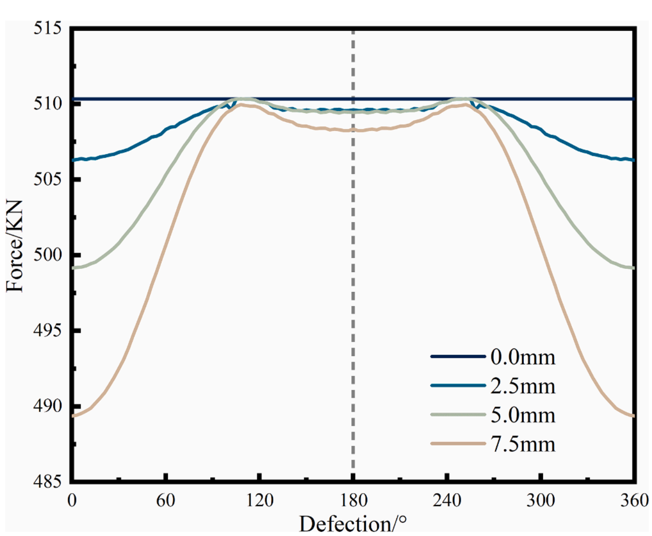

Fig. 16. Correlation between bearing strength and loading angle.

grows up. Hence, the representativeness of the mean CCFST strength will be weaken when the coronal gap reaches a relatively large height. At this moment, the inclination between the loading direcion and the void axis plays an important role in governing the CCFST strength.

Fig. 19 illustrates the influence of the coronal gap height (g) on the different CCFST strength indices under eccentric compression. In Fig. 19 **(a)-(c)**, the longitudinal axis represents the maximum strength, the minimum strength and the mean strength, respectively. The shapes of the 95% confidence intervals indicates that the changing range of the three strength indices gradually increase and the minimum strength decreases quickly as the coronal gap height rising. The fitting curves are deduced when the mean squared error (R^2) $\geq$0.999 as expressed in Eq. (20).

$$\begin{cases} f = -0.034g + 510.335 & (Maximumstrength) \\ f = -2.555g + 510.333 & (Minimumstrength) \\ f = -0.879g + 510.333 & (Meanstrength) \end{cases} \tag{20}$$

From Fig. 19**(d)**, it can be seen that the three fitting curves divide the strength space into four different zones. For actual engineering design, it is the most reasonable and acceptable to select the first and second highest strength zones for the perspective of safety and stability. During the maintenance and management of CCFST structures, the strength

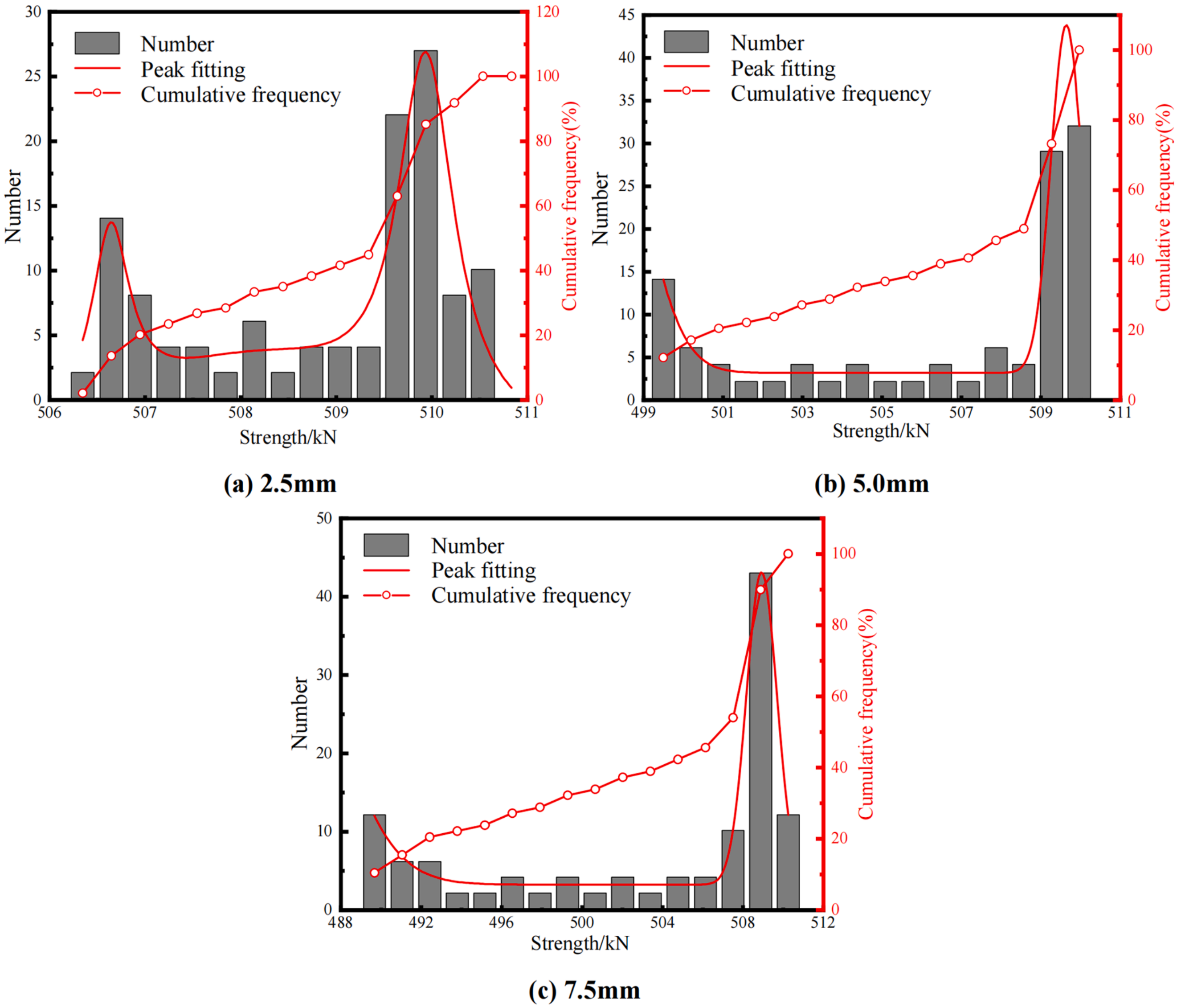

Fig. 17. Probability density of the CCFST strengths under different coronal gap heights.

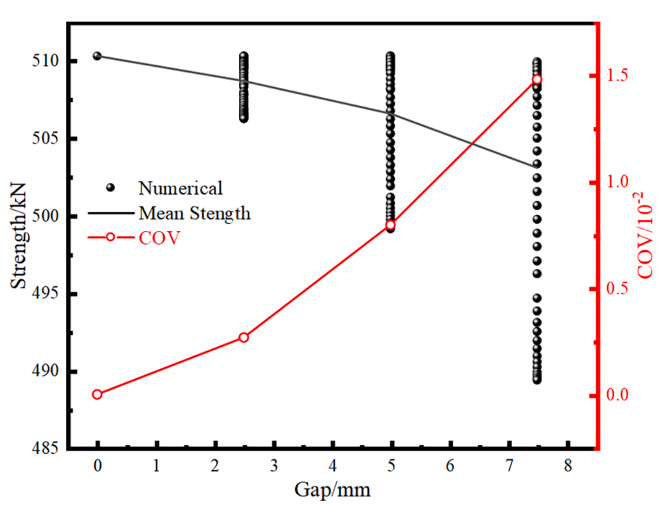

Fig. 18. Variation of strength, mean strength and COV under different coronal gap heights.

indices should be evaluated regularly. Attention should be paid when the measured strength drops to the third highest strength zone, and appropriate reinforcement measures must be taken when the measured strength decreases to the lowest strength zone.

4. Conclusions

In this study, to understand the influence of friction on the shear-slip behavior of heterogeneous brittle composites, a novel cohesive interlayer model has been proposed based on the classical PPR cohesive model. Meanwhile, the capability of the proposed model in dealing with unloading and reloading was improved. By comparing the shear deformation results of a masonry wallette obtained by simulation and experiment, the effectiveness and validity of the proposed model was verified. Then, the coupled model was used to investigate the mechanical response of the circular concrete-filled steel tube under eccentric compression. The main conclusions can be summarized as follows:

(1) Based on the classical PPR cohesive model, a novel cohesive interlayer model has been proposed, and it ensures that friction and cohesion can reach their peaks at the same element deformation. Meanwhile, the unified potential energy function that

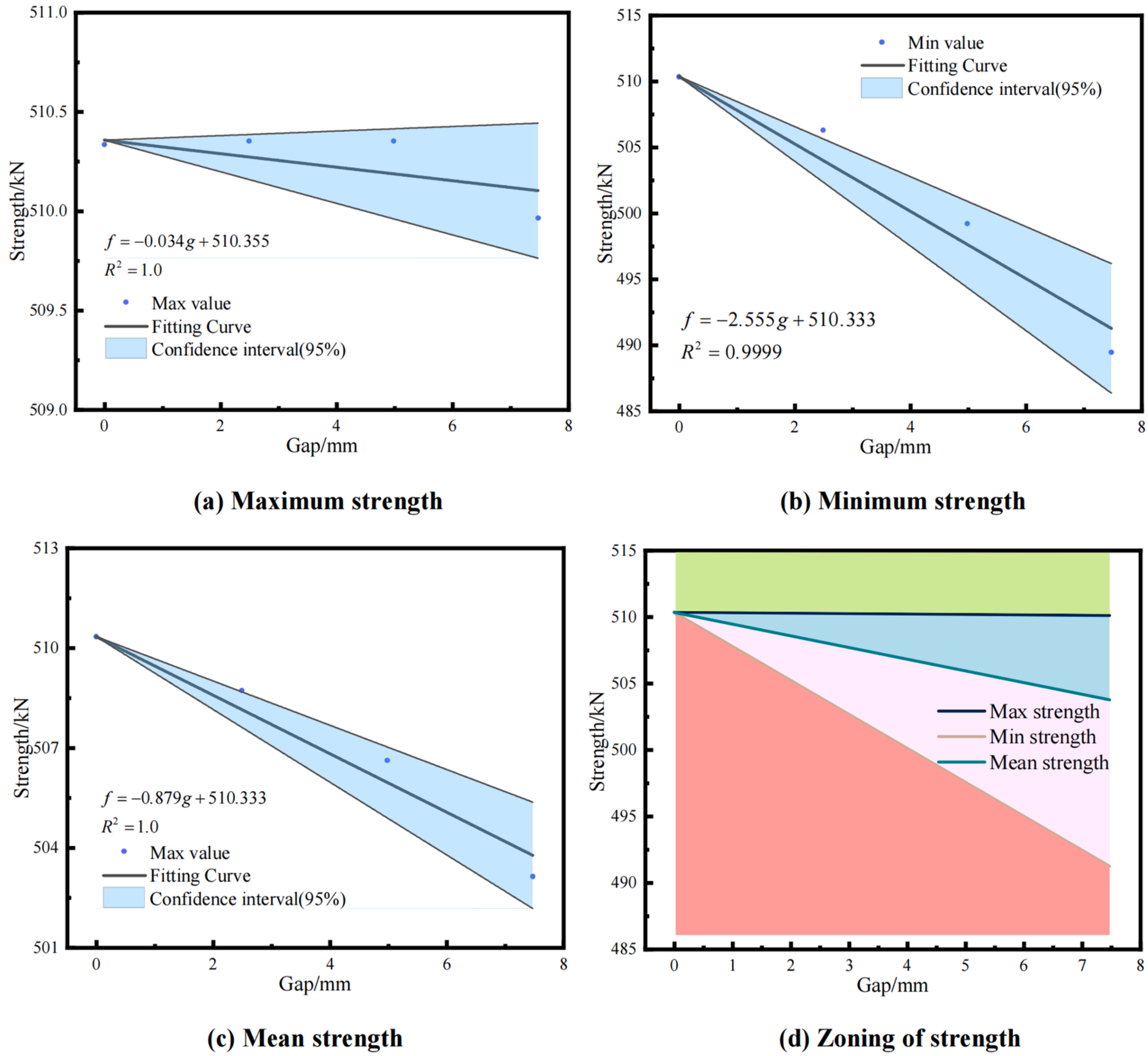

Fig. 19. Influence of the coronal gap height on the different CCFST strength indices under eccentric compression.

governs the tangential and normal behaviors of the interface was introduced to realize the mechanical interaction between Mode I fracture and Mode II fracture. Furthermore, a smooth friction growth function was added in the elastic deformation stage for calculating the accurate contact pressure and friction force, and the difficulty was also solved that the contact surfaces may invade each other excessively which could result in incorrect deformation results.

(2) The capability of the proposed model in addressing unloading and reloading has been improved, and the fracture energy can vary accordingly during cyclic loading. The simulated results indicate that the developed coupling cohesion-friction model can effectively capture the role of friction, especially the jumping behavior of friction under cyclic loading. Simultaneously, the simulated shear stress-displacement curve of the masonry wallette agrees with the related experiment and the other simulations, demonstrating the validity and correctness of the proposed coupling model.

(3) For the shear test of masonry wallette, the relative error of the proposed model is 14.92% which is much lower than those of the three pre-existing models when calculating the displacement corresponding to peak shear stress. In terms of peak shear stress and initial displacement at residual stage, the relative errors of the proposed model are only 1.82% and 5.04%, indicating the high accuracy. Besides, the peak shear stress of the proposed model occurs at a small displacement because the peaks of friction and cohesive are set to be synchronous, facilitating the effective control of the peaks and their corresponding displacements during the parameter fitting.

(4) Under eccentric compression, although the average peak bearing forces of the CCFST structures almost remain at the same level for different coronal gap heights, the fluctuation ranges of the initial deformation modulus, peak bearing force and residual strength are enlarged as the coronal gap height grows up. Simultaneously, when the loading angle increases from 0° to 108°, the compression strength continuously rises to the maximum value. However, it starts to drop with the loading angle keeping increasing and reaches a trough when the loading angle is 180°. Additionally, the probability density of the eccentric compressive strengths follows the bimodal pattern, *i.e.*, the slow growth in the early stage and the rapid growth in the late stage.

CRediT authorship contribution statement

Jiang Yu: Writing – original draft, Visualization, Investigation, Formal analysis, Data curation. **Bin Gong:** Writing – review & editing, Supervision, Methodology, Conceptualization. **Chenrui Cao:** Writing – review & editing, Validation, Formal analysis. **Chun'an Tang:** Supervision, Funding acquisition.

Declaration of competing interest

The authors declare that they have no known competing financial interests or personal relationships that could have appeared to influence the work reported in this paper.

Data availability

Data will be made available on request.

Acknowledgement

This work was financially supported by the National Natural Science Foundation of China (Grant No. 41941018).

Appendix

The algorithm for calculating the normal and tangential cohesive behaviors and frictional jump is shown as follows:
%Normal behavior:
if ($\varDelta_n < 0$) then $T_n = \frac{\partial T_n(0,0)}{\partial \Delta_n}\Delta_n$ %Compression
else if ($0 \le \varDelta_n < \delta_n$ and $|\varDelta_t| < \delta_t$ and $\varDelta_n > \varDelta_{nmax}$) then $T_n = \frac{\partial \psi(\Delta_n, \Delta_t)}{\partial \Delta_n}$ %Elastic and softening.
else if ($0 \le \varDelta_n < \delta_n$ and $|\varDelta_t| < \delta_t$ and $\varDelta_n < \varDelta_{nmax}$) then $T_n = T_n^v(\Delta_{n_{\max}}, \Delta_t)\left(\frac{\Delta_n}{\Delta_{n_{\max}}}\right)^{\alpha_v}$ %Unloading and reloading.
else if ($\varDelta_n \ge \delta_n$ or $|\varDelta_t| \ge \delta_t$) then $T_n = 0$ %Failure.
end if.
%Tangential behavior:
if ($\varDelta_n < 0$) then %Compression
if ($0 \le \varDelta_t < \delta_t$ and $|\varDelta_t| > \varDelta_{tmax}$) then $T_t = \frac{\partial \psi(\Delta_n, \Delta_t)}{\partial \Delta_t} + \mu\kappa(\Delta_t)|T_n|\frac{\partial \Delta_t}{\partial |\Delta_t|}$ %Elastic, softening and friction
else if ($0 \le \varDelta_t < \delta_t$ and $|\varDelta_t| < \varDelta_{tmax}$) then $T_t = T_t^v(\Delta_n, \Delta_{t_{\max}}) + \mu\kappa(\Delta_t)|T_n|\frac{\partial \Delta_t}{\partial |\Delta_t|}$ %Unloading, reloading and friction
else $T_t = \mu\kappa(\Delta_t)|T_n|\frac{\partial \Delta_t}{\partial |\Delta_t|}$ %Failure and friction
end if.
else if ($0 \le \varDelta_n < \delta_n$) then %Tension
if ($0 \le \varDelta_t < \delta_t$ and $|\varDelta_t| > \varDelta_{tmax}$) then $T_t = \frac{\partial \psi(\Delta_n, \Delta_t)}{\partial \Delta_n}$ %Elastic and softening.
else if ($0 \le \varDelta_t < \delta_t$ and $|\varDelta_t| < \varDelta_{tmax}$) then $T_t = T_t^v(\Delta_n, \Delta_{t_{\max}})$ %Unloading and reloading.
else $T_t = 0$ %Failure.
end if.
else if ($\varDelta_n \ge \delta_n$) then $T_t = 0$ %Failure.
end if.

References

Baek, H., Park, K., 2018. Cohesive frictional-contact model for dynamic fracture simulations under compression. Int. J. Solids Struct. 144–145, 86–99.

Benzeggagh, M.L., Kenane, M., 1996. Measurement of mixed-mode delamination fracture toughness of unidirectional glass/epoxy composites with mixed-mode bending apparatus. Compos. Sci. Technol. 56 (4), 439–449.

Beyer, K., Dazio, A., 2012. Quasi-static monotonic and cyclic tests on composite spandrels. Earthq. Spectra 28 (3), 885–906.

Beyer K, Abo-El-Ezz A, Dazio A. Quasi-static cyclic tests on different types of masonry spandrels. Institute of Structural Engineering, Swiss Federal Institute of Technology Zürich, 2010, Report No 327.

Bolhassani, M., Hamid, A.A., Lau, A.C.W., Moon, F., 2015. Simplified micro modeling of partially grouted masonry assemblages. Constr. Build. Mater. 83, 159–173.

Chen, X., Zhu, Y., Cai, D., Xu, G., Dong, T., 2020. Investigation on interface damage between cement concrete base plate and asphalt concrete waterproofing layer under temperature load in ballastless track. Appl. Sci. 10 (8), 2654.

Dehestani, M., Mousavi, S.S., 2015. Modified steel bar model incorporating bond-slip effects for embedded element method. Constr. Build. Mater. 81, 284–290.

Enayatpour, S., van Oort, E., Patzek, T., 2018. Thermal shale fracturing simulation using the cohesive zone method (CZM). J. Nat. Gas Sci. Eng. 55, 476–494.

Feng, X.H., Gong, B., Cheng, X.F., Zhang, H.H., Tang, C.A., 2022. Anisotropy and microcrack-induced failure precursor of shales under dynamic splitting. Geomat. Nat. Haz. Risk 13 (1), 2864–2889.

Feng, X.H., Gong, B., Liang, Z.Z., Wang, S.Y., Tang, C.A., Li, H., Ma, T., 2024. Study of the dynamic failure characteristics of anisotropic shales under impact Brazilian splitting. Rock Mech. Rock Eng. 57, 2213–2230.

Gilormini, P., Diani, J., 2017. Some features of the PPR cohesive-zone model combined with a linear unloading/reloading relationship. Eng. Fract. Mech. 173, 32–40.

Gong, B., Zhao, T., Thusyanthan, I., Tang, C.A., 2024. Modelling rock fracturing by a novel implicit continuous to discontinuous method. Comput. Geotech. 166, 106035.

Haddad, M., Sepehrnoori, K., 2016. XFEM-based CZM for the simulation of 3D multiple-stage hydraulic fracturing in quasi-brittle shale formations. Rock Mech. Rock Eng. 49, 4731–4748.

Han, L.H., An, Y.F., 2014. Performance of concrete-encased CFST box stub columns under axial compression. J. Constr. Steel Res. 93, 62–76.

Hillerborg, A., Modeer, M., Peterson, P.E., 1976. Analysis of crack formation and crack growth in concrete by means of fracture. Cem. Concr. Res. 6 (6), 773–782.

Jin, L., Liu, M.J., Huang, J.Q., Du, X.L., 2019. Mesoscale modelling of bond failure behavior of ribbed steel bar and concrete interface. Scient. Sin. Technol. 49, 445–454.

Kabir, M.I., Lee, C.K., Rana, M.M., Zhang, Y.X., 2019. Flexural and bond-slip behaviours of engineered cementitious composites (ECC) encased steel composite beam. J. Constr. Steel Res. 157, 229–244.

Lee, J., Fenves, G.L., 1998. Plastic-damage model for cyclic loading of concrete structures. J. Eng. Mech. 124 (8), 892–900.

Li, Y., Deng, J.G., Liu, W., Feng, Y., 2017. Modeling hydraulic fracture propagation using cohesive zone model equipped with frictional contact capability. Comput. Geotech. 91, 58–70.

Li, Y., Liu, W., Deng, J., Yang, Y., Zhu, H., 2019. A 2D explicit numerical scheme-based pore pressure cohesive zone model for simulating hydraulic fracture propagation in naturally fractured formation. Energy Sci. Eng. 7 (5), 1527–1543.

Lubliner, J., Oliver, J., Oller, S., Oñate, E., 1989. A plastic-damage model for concrete. Int. J. Solids Struct. 25 (3), 299–326.

Luo, N., Zhang, H., Chai, Y., Li, P., Zhai, C., Zhou, J., Ma, T., 2023. Research on damage failure mechanism and dynamic mechanical behavior of layered shale with different angles under confining pressure. Deep Underground Sci. Eng. 2 (4), 337–345.

Mander, J.B., Priestley, M., 1988a. Observed stress-strain behavior of confined concrete. J. Struct. Eng. 114 (8), 22687.

Mander, J.B., Priestley, M., 1988b. Theoretical stress-strain model for confined concrete. J. Struct. Eng. 114 (8), 1804–1826.

Nasiri, E., Liu, Y., 2017. Development of a detailed 3D FE model for analysis of the in-plane behaviour of masonry infilled concrete frames. Eng. Struct. 143, 603–616.

Oliver, G.L., Paulino, G.H., Buttlar, W.G., 2019. Fractional calculus derivation of a rate-dependent PPR-based cohesive fracture model: theory, implementation, and numerical results. Int. J. Fract. 216, 1–29.

Park, K., 2009. Potential-based fracture mechanics using cohesive zone and virtual internal bond modeling. University of Illinois at Urbana-Champaign. Ph.D. Thesis.

Park, K., Choi, H., Paulino, G.H., 2016. Assessment of cohesive traction-separation relationships in ABAQUS: A comparative study. Mech. Res. Commun. 78, 71–78.

Park, K., Paulino, G.H., 2012. Computational implementation of the PPR potential-based cohesive model in ABAQUS: Educational perspective. Eng. Fract. Mech. 93, 239–262.

Park, K., Paulino, G.H., Roesler, J.R., 2009. A unified potential-based cohesive model of mixed-mode fracture. J. Mech. Phys. Solids 57 (6), 891–908.

Rezazadeh, M., Carvelli, V., Veljkovic, A., 2017. Modelling bond of GFRP rebar and concrete. Constr. Build. Mater. 153, 102–116.

Snozzi, L., Molinari, J.F., 2013. A cohesive element model for mixed mode loading with frictional contact capability. Int. J. Numer. Meth. Eng. 93 (5), 510–526.

Spring, D.W., Paulino, G.H., 2014. A growing library of three-dimensional cohesive elements for use in ABAQUS. Eng. Fract. Mech. 126, 190–216.

Spring, D.W., Paulino, G.H., 2015. Computational homogenization of the debonding of particle reinforced composites: the role of interphases in interfaces. Comput. Mater. Sci 109, 209–224.

Sunkpal, M., Sherizadeh, T., 2022. Exploring the deformation mechanics of coal ribs using the distinct element modeling approach. Rock Mech. Rock Eng. 55, 2879–2898.

Tao, Z., Song, T.Y., Uy, B., Han, L.H., 2016. Bond behavior in concrete-filled steel tubes. J. Constr. Steel Res. 120, 81–93.

Tarasov, B.G., 2023. Fan-hinged shear instead of frictional stick–slip as the main and most dangerous mechanism of natural, induced, and volcanic earthquakes in the earth's crust. Deep Underground Sci. Eng. 2 (4), 305–336.

Tian, L.M., Kou, Y.F., Lin, H.L., Li, T.J., 2021. Interfacial bond-slip behavior between H-shaped steel and engineered cementitious composites (ECCs). Eng. Struct. 231, 111731.

Tvergaard, V., 1990. Effect of fiber debonding in a whisker-reinforced metal. Mater. Sci. Eng. A 125 (2), 203–213.

Wang, Y.Y., Gong, B., Tang, C.A., 2022. Numerical investigation on anisotropy and shape effect of mechanical properties of columnar jointed basalts containing transverse joints. Rock Mech. Rock Eng. 55, 7191–7222.

Wang, Y.F., Ma, Y.S., Han, B., Deng, S.Y., 2013. Temperature effect on creep behavior of CFST arch bridges. J. Bridg. Eng. 18 (12), 1397–1405.

Yang, J., Lian, H., Nugyen, V.P., 2021. Study of mixed mode I/II cohesive zone models of different rank coals. Eng. Fract. Mech. 246, 107611.

Yao, Y., Liu, L., Keer, L.M., 2015. Pore pressure cohesive zone modeling of hydraulic fracture in quasi-brittle rocks. Mech. Mater. 83, 17–29.

Yu, M., Yang, B., Chi, Y., Xie, J., Ye, J., 2020. Experimental study and DEM modelling of bolted composite lap joints subjected to tension. Compos. B Eng. 190, 107951.

Zeng, B., Li, Y., Noguez, C.C., 2021. Modeling and parameter importance investigation for simulating in-plane and out-of-plane behaviors of un-reinforced masonry walls. Eng. Struct. 248, 113233.

Zhang, M., Yu, J., Guo, C., 2020. Numerical simulation of interlaminar shear test between asphalt concrete and inorganic binder based on cohesive model. Sci. Technol. Eng. 20 (32), 13417–13424.

Zhong, Y., Gao, L., Cai, X., An, B., Zhang, Z., Lin, J., Qin, Y., 2021. An improved cohesive zone model for interface mixed-mode fractures of railway slab tracks. Appl. Sci. 11 (1), 456.